




TOOLS

Engineered synaptic tools reveal localized cAMP signaling in synapse assembly

Richard Sando^{1,2,3} , Milan Lyndie Ho^{1,2}, Xinran Liu⁴ , and Thomas C. Südhof^{1,2} 

The physiological mechanisms driving synapse formation are elusive. Although numerous signals are known to regulate synapses, it remains unclear which signaling mechanisms organize initial synapse assembly. Here, we describe new tools, referred to as “SynTAMs” for synaptic targeting molecules, that enable localized perturbations of cAMP signaling in developing postsynaptic specializations. We show that locally restricted suppression of postsynaptic cAMP levels or of cAMP-dependent protein-kinase activity severely impairs excitatory synapse formation without affecting neuronal maturation, dendritic arborization, or inhibitory synapse formation. In vivo, suppression of postsynaptic cAMP signaling in CA1 neurons prevented formation of both Schaffer-collateral and entorhinal-CA1/temporoammonic-path synapses, suggesting a general principle. Retrograde trans-synaptic rabies virus tracing revealed that postsynaptic cAMP signaling is required for continuous replacement of synapses throughout life. Given that postsynaptic latrophilin adhesion-GPCRs drive synapse formation and produce cAMP, we suggest that spatially restricted postsynaptic cAMP signals organize assembly of postsynaptic specializations during synapse formation.

Introduction

Synapse formation is tightly orchestrated to achieve the precisely coordinated development of pre- and postsynaptic specializations, leading to the precise assembly of neural circuits. Synapse formation is likely controlled by activation of surface receptors such as adhesion molecules that stimulate intracellular signal transduction pathways. Key adhesion molecules in synapse formation, such as latrophilins (Sando and Südhof, 2021; Araç and Li, 2019; Südhof, 2018), were recently identified, but the intracellular signals that drive synapse formation are poorly understood (Sanes and Yamagata, 2009; Ribic and Biederer, 2019; Lie et al., 2018; de Wit and Ghosh, 2016; Südhof, 2021; Nusser, 2018). In fact, no specific intracellular signaling pathway has been shown at this point to be required for synapse formation in any system, although regulatory mechanisms such as ubiquitination were demonstrated to contribute to synapse stability (Collins et al., 2006; Russo et al., 2019; Wan et al., 2000).

Most synapse formation in vertebrates occurs postnatally after neurons have migrated to their final positions in the brain, elaborated dendritic arbors, and extended axons to their target regions. In mammals, a remarkable phase of exuberant synapse formation during the postnatal period produces a vast excess of synapses that are subsequently pruned. In the human cortex, for

example, a phase of rapid synapse formation during the first decade of life is followed by a prolonged period of elimination that decreases the total number of synapses by ~50% (Huttenlocher et al., 1982; Bourgeois and Rakic, 1993; Petanjek et al., 2011). Moreover, although overall synapse numbers are stable when an animal reaches adulthood, synapses themselves are not. Synapses are continuously remodeled, eliminated, and newly formed throughout life. In some brain areas, most notably the CA1 region of the hippocampus, synapses are replaced at a high rate. Strikingly, ~40% of synapses on CA1 region neurons are eliminated and reformed in 4 d, with nearly all replaced in a matter of weeks (Attardo et al., 2015; Pfeiffer et al., 2018; Wiegert et al., 2018). Other brain areas, such as the sensory cortex, exhibit a lower rate of synapse elimination and formation, but here too synapses turn over continuously (Attardo et al., 2015; Qiao et al., 2016). Thus, different from neurogenesis and axon guidance, overall synapse formation represents not only a developmental process but also an ongoing mechanism of circuit reconstruction throughout life.

Recent studies identified key cell-surface molecules that contribute to controlling synapse formation, such as neurexins and their numerous ligands, synaptic adhesion-like molecules, leukocyte common antigen-related-type receptor-type tyrosine-

¹Department of Molecular and Cellular Physiology, Stanford University School of Medicine, Stanford, CA; ²Howard Hughes Medical Institute, Stanford University School of Medicine, Stanford, CA; ³Department of Pharmacology, Vanderbilt University, Nashville, TN; ⁴Department of Cell Biology, Yale University School of Medicine, New Haven, CT.

Correspondence to Richard Sando: richard.sando@vanderbilt.edu; Thomas C. Südhof: tcsl@stanford.edu.

© 2021 Sando et al. This article is distributed under the terms of an Attribution–Noncommercial–Share Alike–No Mirror Sites license for the first six months after the publication date (see <http://www.rupress.org/terms/>). After six months it is available under a Creative Commons License (Attribution–Noncommercial–Share Alike 4.0 International license, as described at <https://creativecommons.org/licenses/by-nc-sa/4.0/>).



protein phosphatases, latrophilins, and Bai's (reviewed in [Lie et al., 2018](#); [Biederer et al., 2017](#); [Connor et al., 2019](#); [Südhof, 2017](#); [Jang et al., 2017](#); [Suzuki et al., 2020](#); [Yuzaki, 2018](#); [Kasem et al., 2018](#)). However, the signals produced by activation of these and other molecules that control synapse formation remain enigmatic. Latrophilins increase cAMP synthesis ([Sando and Südhof, 2021](#)), but whether cAMP is involved in synapse formation, as opposed to axonal pathfinding before synapse formation ([Song et al., 1997](#); [Höpker et al., 1999](#); [Imai et al., 2006](#); [Shelly et al., 2010](#)) or long-term plasticity after synapse formation ([Weisskopf et al., 1994](#); [Hashimoto et al., 2017](#); [Chevalere et al., 2007](#); [Hopkins and Johnston, 1988](#); [Frey et al., 1993](#); [Bolshakov et al., 1997](#); [Deisseroth et al., 1996](#)), is unknown. If we are to understand how circuits are constructed in the brain and how they are continuously remodeled throughout life, insight into the cell biology of synapse formation and the signaling cascades that drive the assembly of various synaptic components will be essential ([Südhof, 2021](#)).

Signals driving synapse formation must be highly localized and spatially restricted to nascent synaptic junctions. However, no current technologies enable facile, localized perturbations of specific signals in developing pre- or postsynaptic compartments. Here, we report the development of SynTAMs (synaptic targeting molecules) that enable specific perturbations in developing postsynaptic specializations. We focused on cAMP signaling because previous findings suggest that cAMP signaling via protein kinase-A (PKA) may be involved in synapse formation. [Kwon and Sabatini \(2011\)](#) observed that in cultured slices, acute photolysis of caged glutamate induces formation of dendritic spines associated with synapses and that spine formation was blocked by a PKA inhibitor, suggesting that cAMP signaling via PKA may be important for synapse formation. Moreover, we found that pharmacological inhibitors of cAMP signaling impair heterologous synapse induction on nonneuronal cells expressing a synaptogenic cell-surface protein ([Jiang et al., 2021](#)).

Here, we show that SynTAMs that selectively suppress localized cAMP signaling at nascent postsynaptic sites also severely impair synapse assembly. Our results report a new set of tools that can be adapted to different signaling pathways and reveal a central role for continuous cAMP signaling in synapse assembly in cultured neurons and in vivo. Since synapses are continuously eliminated and replaced ([Attardo et al., 2015](#); [Pfeiffer et al., 2018](#)), the organizational signaling function of cAMP may thus represent a general principle that operates throughout the life of an organism.

Results

Design of SynTAM tools suppressing local postsynaptic cAMP signaling

Based on the observations that PKA inhibitors block spine formation induced by acute application of glutamate ([Kwon and Sabatini, 2011](#)), that PKA contributes to signaling in heterologous synapse formation ([Jiang et al., 2021](#)), and that latrophilins can stimulate cAMP production and are essential for synapse formation ([Sando and Südhof, 2021](#)), we set out to explore the possibility that cAMP acts as a signal promoting synapse

formation. However, pharmacological and genetic manipulations of cAMP-dependent signaling affect all subcellular compartments and influence multitudinous cellular processes, whereas physiological cAMP signaling is spatially restricted in neurons ([Gorshkov et al., 2017](#); [Averaimo and Nicol, 2014](#); [West et al., 2001](#); [Argyrousi et al., 2020](#)). A role for cAMP in synapse assembly would thus have to be restricted to the developing synaptic junction, but no tools that enable selective compartmentalized suppression of cAMP levels in postsynaptic specializations are readily available.

To develop such tools, we targeted the cAMP-specific phosphodiesterase PDE7b ([Hetman et al., 2000](#)) or the PKA inhibitor peptide PKI ([Dalton and Dewey, 2006](#)) to excitatory postsynaptic sites ([Fig. 1 a](#)). We fused PDE7b or PKI to Homer1, which is specifically localized at postsynaptic densities ([Xiao et al., 2000](#); [Kennedy, 2000](#); [Worley et al., 2007](#)), resulting in PDE-Hr1 or PKI-Hr1 SynTAMs. As controls, we used PDE7b expressed alone without fusion to a targeting domain (PDE) or a Homer1 fusion of mutant PDE7b that is catalytically inactive (PDE*-Hr1). In addition, we developed a second class of SynTAMs in which PDE7b is targeted to postsynaptic densities (PSDs) by attaching it to nanobodies that are directed to Homer1 ([Fig. 1 a](#); see below). cAMP measurements confirmed that the Homer1- and nanobody-PDE fusion proteins were enzymatically active ([Fig. S1, a-d](#)).

When expressed in neurons, both PDE-Hr1 and PDE*-Hr1 were quantitatively localized to the postsynaptic density of excitatory synapses in dendritic spines ([Fig. 1 b](#) and [Fig. S1](#)). PDE7b expressed alone without a fusion partner was present in the soma and proximal dendrites but was de-enriched in distal dendrites and not detectable in spines ([Fig. S1, i-j](#)). The PKI-Hr1 SynTAM was also localized to postsynaptic sites, enabling specific inhibition of PKA at developing synapses ([Fig. S1 m](#)). Thus, these new tools target a cargo (PDE7b or PKI) to postsynaptic specializations, enabling specific manipulations of postsynaptic cAMP signaling in nascent synapses ([Fig. 1 a](#)).

SynTAMs that suppress postsynaptic cAMP signaling impair synapse formation

We expressed PDE-Hr1 or PKI-Hr1 in cultured hippocampal neurons starting at day in vitro (DIV) 3, before synapses have formed ([Chanda et al., 2017](#)). We then measured the density of spines in biocytin-filled neurons as a proxy of excitatory synapses. Both PDE-Hr1 and PKI-Hr1 caused a large decrease in spine density, measured by confocal microscopy and EM ([Fig. 1, c-f](#)). PKI-Hr1 was less effective than PDE-Hr1, presumably because PKI is a stoichiometric PKA inhibitor and not an enzyme hydrolyzing cAMP ([Fig. 1, c and d](#)). EM analyses confirmed that the PDE-Hr1 SynTAM decreased synapse density ([Fig. 1, g and h](#)) and revealed that the remaining synapses exhibited a significant decrease in the width and thickness of PSDs without a presynaptic change ([Fig. 1, i and j](#); and [Fig. S2, c and d](#)). Thus, the remaining synapses that are still formed after suppression of postsynaptic cAMP levels have smaller synaptic junctions. Moreover, we measured the effect of PDE-Hr1 on dendritic development but found no impairments ([Fig. S2, a and b](#)).

These data suggest that PDE-Hr1 and PKI-Hr1 impair synapse formation, such that some synapses do not form while the

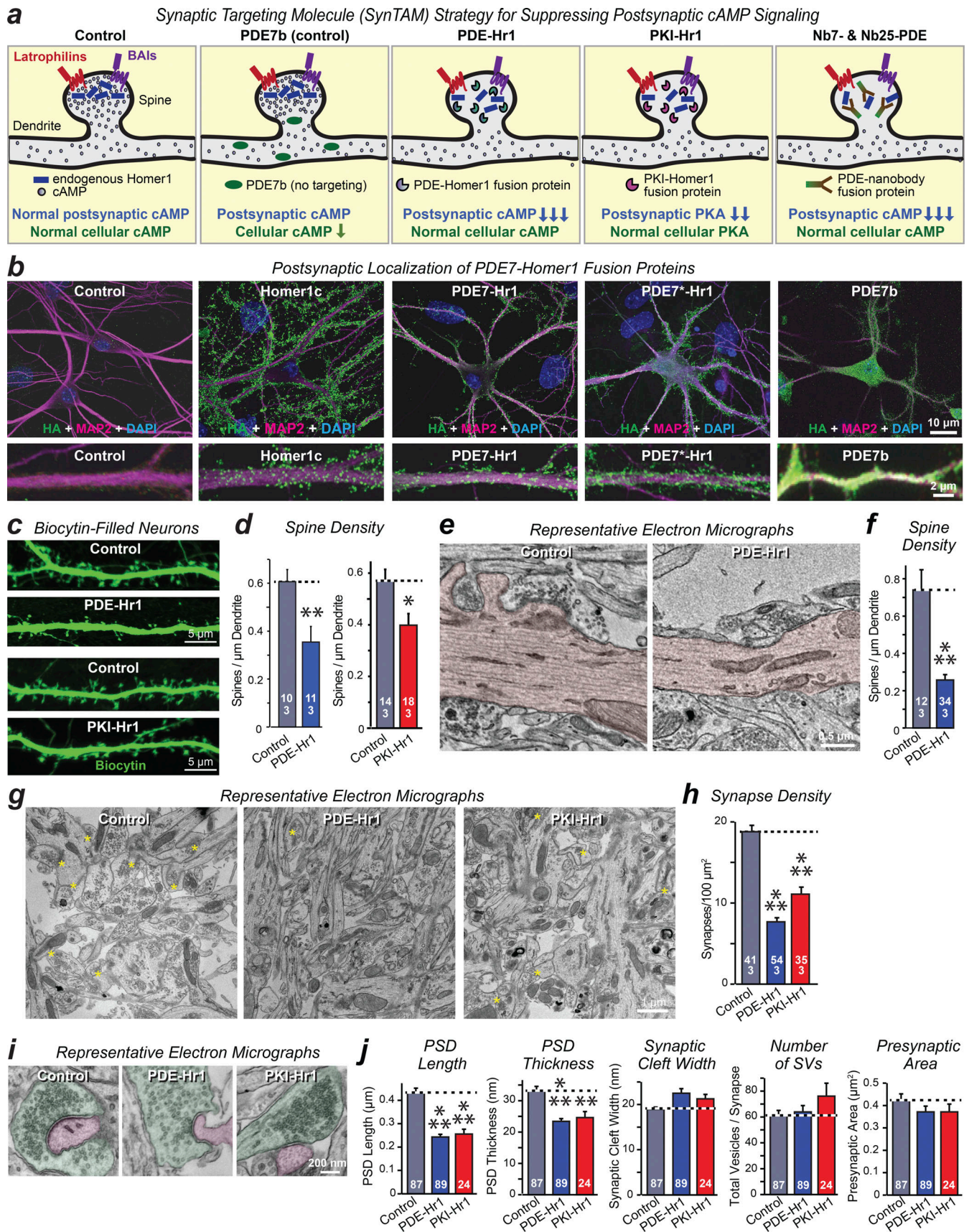


Figure 1. **SynTAMs that suppress postsynaptic cAMP signaling impair synapse formation in cultured hippocampal neurons.** (a) Diagram of SynTAM designs. The two different SynTAM classes differ in how a cargo is targeted to nascent postsynaptic specializations. In PDE-Hr1 and PKI-Hr1 SynTAMs, the

cargo is fused to Homer1c, whereas in Nb7- and Nb25-PDE SynTAMs, the cargo is attached to nanobodies specific for Homer1. Controls consist of nontargeted PDE7b or SynTAMs containing catalytically inactive PDE7b mutants (PDE*-Hr1). **(b)** PDE-Hr1 and PDE*-Hr1 are specifically targeted to developing postsynaptic specializations in cultured hippocampal neurons, whereas PDE7b diffuses to the soma and primary dendrites. Neurons were infected with lentiviruses encoding the indicated HA-tagged cDNAs at DIV3 and stained for various HA-tagged proteins, MAP2, and DAPI at DIV14–16 (top: overview; bottom: higher-magnification images; all proteins were HA-tagged; “Control” = infection with empty lentiviral particles packaged in parallel with test lentiviruses). **(c and d)** Local suppression of postsynaptic cAMP levels with PDE-Hr1 or postsynaptic PKA signaling with PKI-Hr1 decreases spine density in cultured hippocampal neurons. **(c)** Representative confocal images of dendrites in control neurons or neurons expressing PDE-Hr1 or PKI-Hr1 that were filled with biocytin via a patch pipette. **(d)** Quantifications of total spine density in PDE-Hr1 experiments (left) and PKI-Hr1 experiments (right). **(e–h)** EM confirms that local postsynaptic cAMP depletion decreases spine density (representative images, e; summary graph, f) and synapse density in cultured hippocampal neurons (representative images, g; summary graph, h). Yellow asterisks denote synaptic junctions. **(i and j)** Ultrastructural analysis of pre- and postsynaptic parameters by EM shows that postsynaptic cAMP depletion alters the size of PSDs in surviving synapses but has no significant effect on presynaptic parameters. (representative images of individual synapses [i; green, presynaptic terminals; pink, postsynaptic spines]; summary graphs of indicated parameters; j). Data are means \pm SEM (numbers in bars: d, f, h = numbers of cells/experiments and j = number of analyzed synapses). Statistical significance was assessed by two-tailed t test or one-way ANOVA with post hoc Tukey tests for multiple comparisons (***, $P < 0.001$; **, $P < 0.01$; *, $P < 0.05$). For additional data, see Fig. S1 and Fig. 2. BAI, brain angiogenesis inhibitor; SV, synaptic vesicle.

residual synapses are structurally altered. To assess synaptic function, we monitored spontaneous miniature excitatory postsynaptic currents (mEPSCs) and miniature inhibitory postsynaptic currents (mIPSCs) whose frequency is, among others, a measure of excitatory and inhibitory synapse density. PDE-Hr1 severely suppressed the mEPSC frequency and caused a modest decrease in the mEPSC amplitude (Fig. 2, a–c). Neither PDE alone nor inactive PDE*-Hr1 changed the mEPSC frequency or amplitude (Fig. 2, a–c). Importantly, none of these manipulations altered mIPSCs (Fig. 2, d–f), consistent with the selective targeting of PDE-Hr1 to excitatory synapses (Fig. S1 k). Similarly, PKI-Hr1 suppressed mEPSC frequency and amplitude, confirming that the cAMP–PKA signaling pathway is the target of the PDE-Hr1 manipulation (Fig. 2, g–i). The specificity of this effect on excitatory synapses was further validated by the finding that capacitance or input resistance was unaltered (Fig. S2, e and f).

These results suggest that selective suppression of cAMP signaling at postsynaptic sites decreases formation of functional synapses. However, it is also possible that cAMP serves as a survival signal (i.e., that synapses are formed and mature normally but are later destabilized and eliminated in the absence of cAMP signaling). To test this possibility, we asked whether PDE-Hr1 prevents the development of functional synapses, monitored via mEPSCs, or secondarily destabilizes synapses after formation (Fig. 2 j). In control neurons, we observed few mEPSCs at DIV6, more frequent mEPSCs at DIV8, and maximal numbers of mEPSCs at DIV12 (Fig. 2 j), consistent with earlier results (Chanda et al., 2017). Suppression of postsynaptic cAMP signaling with PDE-Hr1 SynTAMs prevented the initial emergence of mEPSCs, and peak mEPSC activity at DIV12 was decreased by ~75% (Fig. 2, k and l). These data suggest that PDE-Hr1 SynTAMs prevented formation of functional synapses. The residual synapses remaining after suppression of cAMP signaling were stable but again exhibited a significant decrease in mEPSC amplitude (Fig. 2l). Importantly, inactive PDE*-Hr1 had no effect, and none of the manipulations altered mIPSCs, confirming specificity (Fig. 2, m and n; and Fig. S2, g–i). Moreover, the neuronal capacitance and input resistance were unchanged (Fig. S2). Thus, suppression of postsynaptic cAMP signaling does not destabilize synapses but impairs their initial formation.

It has been shown that perinuclear cAMP signaling is essential for neuronal survival and axonal development (Boczek

et al., 2019), raising the possibility that the PDE7b activity introduced by the PDE-Hr1 protein could impair neuronal health and thereby decrease synaptic connectivity. Although this possibility seems unlikely given the normal dendritic arborization and unchanged electrical properties of neurons expressing SynTAMs, we addressed this concern with a series of targeting proteins that direct PDE7b to the endoplasmic reticulum, mitochondria, or nucleus instead of PSDs (Fig. 3 a). Expression of these proteins that impair cAMP signaling outside of PSDs did not alter the mEPSC frequency or amplitude in cultured neurons, confirming specificity of SynTAMs (Fig. 3, b–d).

Nanobody-mediated suppression of postsynaptic cAMP signaling also impairs synapse formation

The striking impairment in synapse formation by suppression of postsynaptic cAMP signaling using PDE-Hr1 or PKI-Hr1 differs from previous observations on the role of cAMP in neuronal development, including axon pathfinding (Mai et al., 2009; Shelly et al., 2010; Imai et al., 2006; Höpker et al., 1999; Song et al., 1997) and long-term synaptic plasticity (Frey et al., 1993; Weisskopf et al., 1994; Duffy and Nguyen, 2003; Bolshakov et al., 1997; Yeckel et al., 1999; Chetkovich et al., 1991; Hopkins and Johnston, 1988; Argyrousi et al., 2020). Our various control manipulations show that mIPSCs, dendritic arborization, capacitance, and input resistance are not changed by interfering with localized postsynaptic cAMP signaling (Fig. 1, Fig. 2, Fig. S1, and Fig. S2) and that an effect on synapse formation is only detectable when PDE7b is specifically targeted to developing postsynaptic specializations (Fig. 3). These controls document a synaptic effect. Since PDE-Hr1 and PKI-Hr1 SynTAMs, however, depend on fusion of PDE7b or PKI to Homer1c that then targets this moiety to postsynaptic specializations, it is conceivable that they impair synapse formation because of the overexpression of Homer1c or the combination of Homer1c overexpression with the cAMP manipulation. To control for these possibilities, we developed a second class of SynTAMs that target PDE7b to postsynaptic densities without overexpression of Homer1c and additionally tested the effect of Homer1c overexpression alone.

We tethered PDE to Nb7 and Nb25 nanobodies that bind to endogenous Homer1 in neurons (Dong et al., 2019), creating Nb7-Hr1 and Nb25-Hr1 SynTAMs that latch onto developing postsynaptic densities (see schematic in Fig. 1 a). Immunocytochemistry

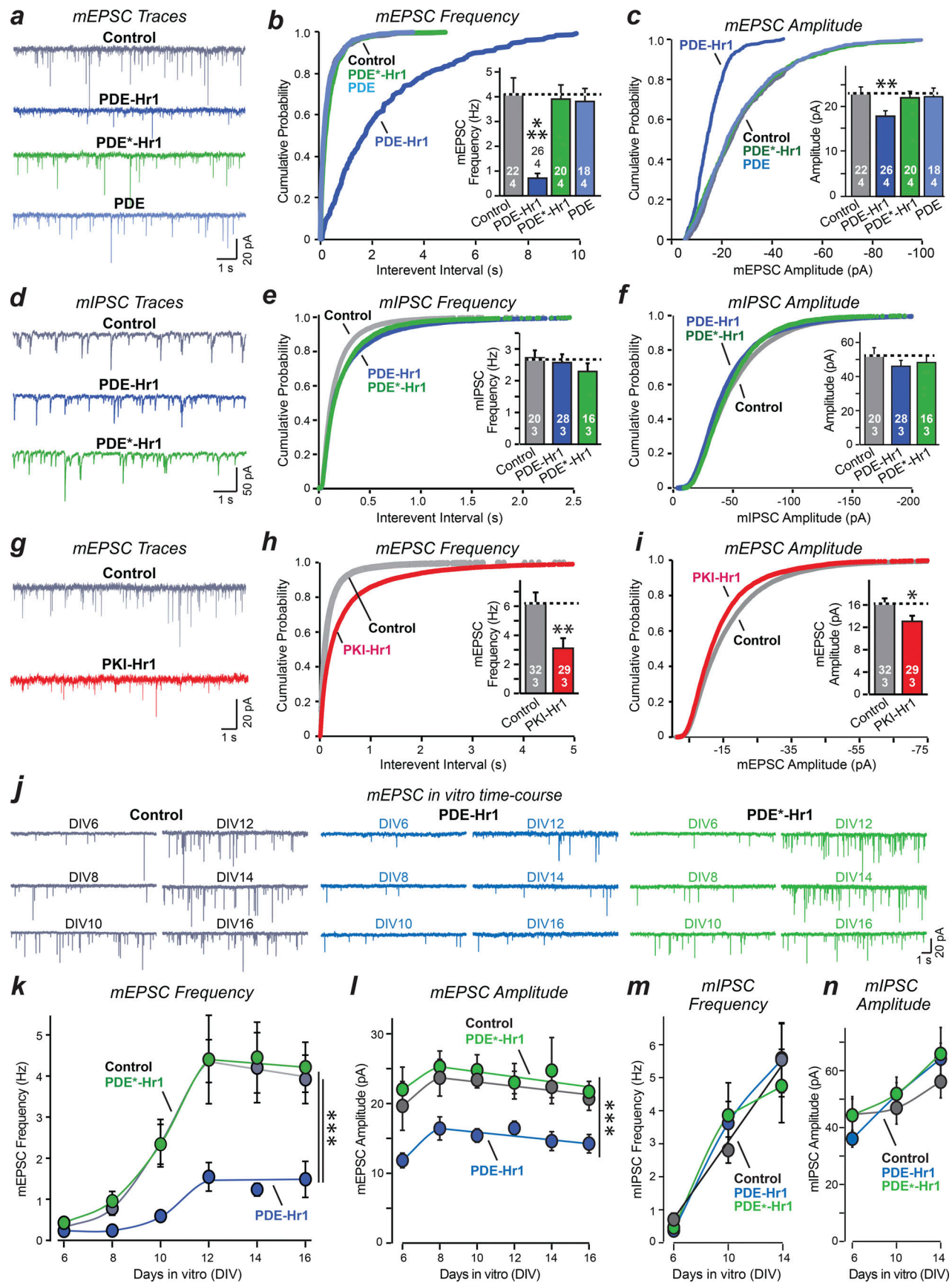


Figure 2. Measurement of mEPSCs and mIPSCs shows that local postsynaptic cAMP suppression impairs functional excitatory synapse formation. (a–c) PDE-Hr1 decreases mEPSC frequency and amplitude. (a) Representative traces. (b) Cumulative probability plot of interevent intervals and summary

graph of the mean mEPSC frequency [inset]. **(c)** Cumulative probability plot and summary graph [inset] of mEPSC amplitude. Neurons were prepared as described for Fig. 1 b. **(d-f)** Postsynaptic cAMP depletion has no effect on mIPSC frequency or amplitude. Same as a-c, except that mIPSCs were monitored. **(g-i)** Postsynaptic inhibition of cAMP-dependent PKA by targeting PKI to the postsynaptic compartment (PKI-Hr1) also suppresses mEPSC frequency. Same as a-c, except that PKI-Hr1 was analyzed. **(j-l)** Local suppression of postsynaptic cAMP levels prevents development of functional synapses as monitored via mEPSCs that were measured as a function of culture time. **(i)** Representative mEPSC traces at the indicated days in vitro [DIV6-DIV16]. **(k)** Summary plot of mEPSC frequency as a function of DIV. Cultured hippocampal neurons were infected with lentiviruses encoding PDE-Hr, PDE*-Hr, and EGFP (control) at DIV0 and analyzed at the indicated culture times. See Fig. S3, a and b for passive electrical properties. **(m and n)** Same as k and l, except mIPSCs were monitored. Fewer developmental time points were analyzed due to the lack of effect of PDE-Hr on mIPSCs. See Fig. S3 c for representative mIPSC traces and Fig. S3, d and e for passive electrical properties. Data are means \pm SEM (numbers of cells/experiments are indicated in bars). Statistical significance was assessed by two-tailed *t* test, one-way ANOVA, or two-way ANOVA with post hoc Tukey tests for multiple comparisons (***, $P < 0.001$; **, $P < 0.01$; *, $P < 0.05$). For additional data, see Fig. S2.

(ICC) with confocal and stochastic optical reconstruction microscopy (STORM) documented that Nb7- and Nb25-based intrabodies are specifically targeted to excitatory synapses and that their expression does not alter the size of these synapses (Fig. 4, a-c; and Fig. S3). Moreover, PDE-nanobodies did not impair the dendritic arborization of neurons (Fig. S2, a and b). EM analyses showed, however, that Nb7-PDE decreased synapse numbers similar to PDE-Hr1 (Fig. 4, d and e). Moreover, Nb7-PDE and Nb25-PDE suppressed the mEPSC

frequency with an efficacy (~85% decrease) comparable to that of PDE-Hr1 (Fig. 4, f and g). In addition, Nb7-PDE and Nb25-PDE caused a decline (~20-35%) in mEPSC amplitude similar to PDE-Hr1 (Fig. 4 h). Overexpression of either Homer1c alone (as an EGFP-fusion protein) or of Nb7 nanobodies alone (as YFP-fusion proteins) had no effect on the mEPSC frequency and amplitude, whereas PDE-Hr1 and Nb7-PDE, examined in the same experiments, suppressed them (Fig. 4, i-k). Similar to PDE-Hr1, Nb7-PDE and Nb25-PDE decreased

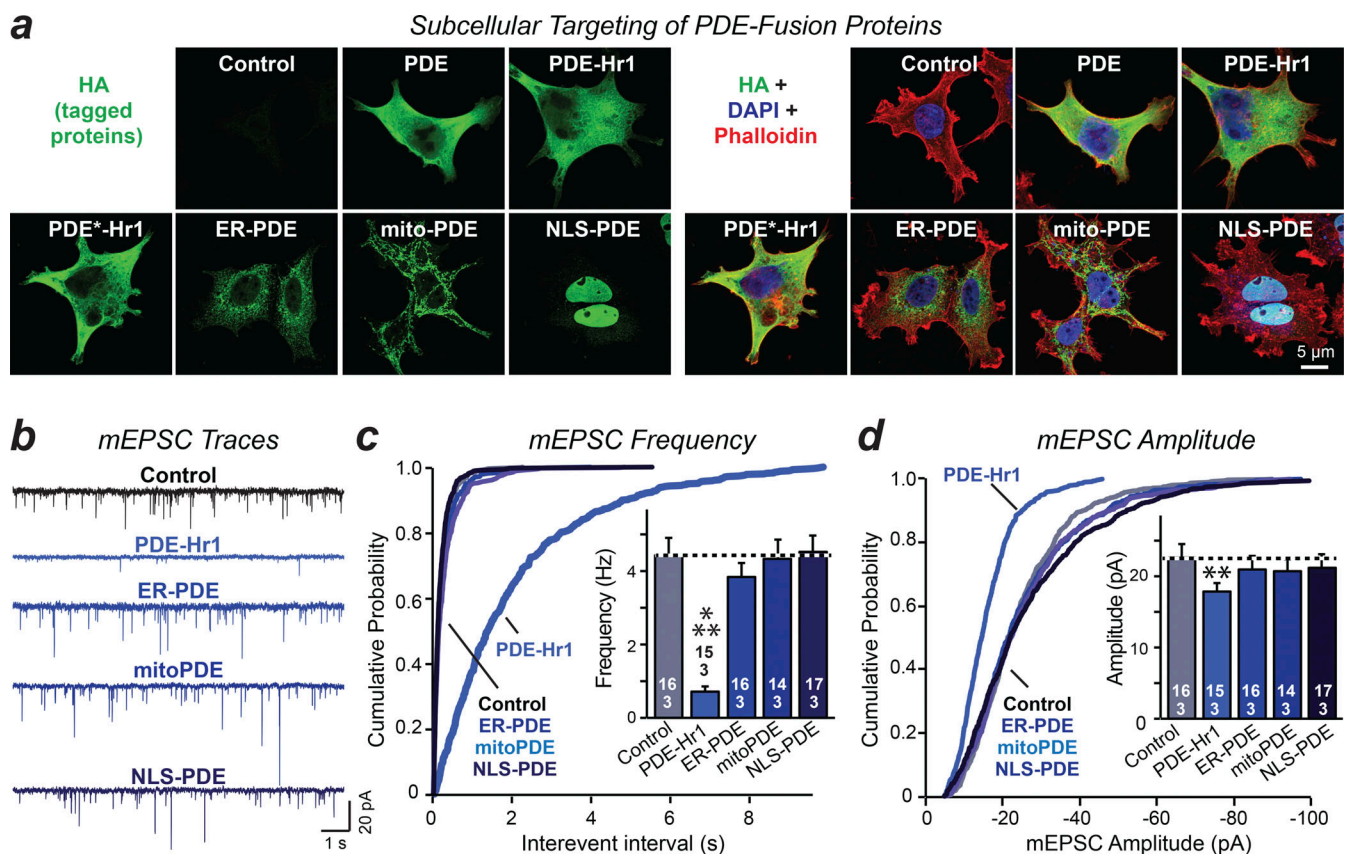


Figure 3. **Suppression of cAMP signaling in other subcellular locations different from developing postsynaptic specializations does not impair excitatory synapses.** **(a)** Representative images of PDE fusion protein localization in HEK293T cells (PDE, HA-tagged PDE7b lacking targeting sequences; PDE-Hr1 and PDE*-Hr1, PDE-fusion proteins with Homer1c that are targeted to synapses; ER-PDE, ER-targeted PDE; mito-PDE, mitochondria-targeted PDE; NLS-PDE, nuclear-targeted PDE). **(b-d)** Suppression of cAMP signaling in developing postsynaptic specializations but not in other subcellular locations impairs synapse formation as monitored by mEPSC measurements. **(b)** Representative mEPSC traces. **(c)** Cumulative probability plots of interevent intervals and summary graph of the mean mEPSC frequency [inset]. **(d)** Cumulative probability plots and summary graph [inset] of mEPSC amplitude. Neurons and Control conditions were prepared as described for Fig. 1 b. Data are means \pm SEM (numbers of cells/experiments are indicated in bars). Statistical significance was assessed by one-way ANOVA with post hoc Tukey tests for multiple comparisons (***, $P < 0.001$; **, $P < 0.01$).

the size and thickness of the postsynaptic density of the remaining synapses as monitored by EM (Fig. S3 c and Fig. 4 d). Thus, ablating postsynaptic cAMP signaling by different approaches suppresses formation of functional excitatory synapses.

Postsynaptic suppression of cAMP signaling impairs synapse formation in vivo

Is local cAMP signaling also involved in synapse formation in vivo? To address this question, we used stereotactic injections in newborn mice to sparsely infect CA1 pyramidal neurons with lentiviruses that coexpress EGFP or tdTomato with PDE-Hr1, inactive PDE*-Hr1, PKI-Hr1, or Nb7-PDE SynTAMs (Fig. S4 a and Fig. 6 b). After 3–4 wk, we prepared acute hippocampal slices from these mice and filled infected and uninfected control neurons with biocytin via a patch pipette for morphological analyses (Fig. 5 a). Reconstruction of dendritic arbors revealed no significant differences in dendritic morphology between control, PDE*-Hr1-, PDE-Hr1-, and PKI-Hr1-expressing neurons (Fig. 5, b and c; Fig. S4 c; and Fig. 6 d). PDE-Hr1, however, decreased the spine density (~55%) in all dendritic domains of CA1 pyramidal neurons (Fig. 5, d and e; and Fig. S4 g). In contrast, catalytically inactive PDE*-Homer1 had no effect.

We subsequently measured synaptic responses. Again, PDE-Hr1 reduced the mEPSC frequency (~50%) and modestly decreased the amplitude of the remaining mEPSCs, whereas the frequency and amplitude of mIPSCs and the electrical properties of neurons were unchanged (Fig. 6, a and b; and Fig. S5, a–c). PKI-Hr1 and Nb7-PDE had similar effects on mEPSCs (Fig. 6, c and d; and Fig. S5, d–f). None of the SynTAMs altered the capacitance or input resistance of neurons (Fig. S5 c and Fig. 5 f). Thus, suppression of cAMP signaling in vivo also inhibits development of functional synapses.

Does SynTAM-mediated suppression of postsynaptic cAMP signaling impair the initial formation of synapses or destabilize synapses after they were formed? To address this central question, we analyzed mEPSCs in acute hippocampal slices from mice during the acute phase of synapse formation and elimination between P6 and P25. We sparsely infected CA1 neurons in newborn mice by stereotactic injections as described above and performed whole-cell patch-clamp recordings in acute slices at P6 (postnatal day 6)–P25 (Fig. S5 g). We found that the capacitance of CA1 neurons steadily increased from ~70 pF to ~160 pF during the P6–P18 time period, documenting CA1 neuron maturation (Fig. 6 e). During this period, the input resistance continuously decreased from ~0.45 G Ω to ~0.15 G Ω , confirming the gradual maturation of CA1 neurons (Fig. 6 f). Suppression of local postsynaptic cAMP levels using PDE-Hr1 had no effect on the developmental increase in capacitance or the decrease in input resistance, suggesting that it does not impair neuronal maturation.

In control neurons, mEPSCs were robustly detected at P6, a time when the neuronal capacitance was <50% and the input resistance was ~300% of a mature neuron (Fig. 6 g). In these control neurons, the mEPSC frequency doubled from P6 to P10 but decreased again from P10 to P18 to the levels observed at P6 (Fig. 6 h), while the mEPSC amplitude remained stable (Fig. 6 i). The dramatic increase and fall in mEPSC frequency during

postnatal development is consistent with the large excess of synapse formation and subsequent synapsin elimination during the normal maturation of the brain (Huttenlocher et al., 1982; Bourgeois and Rakic, 1993; Petanjek et al., 2011). In mice expressing PDE-Hr1, the mEPSC frequency was significantly decreased (~45%) at P6, and the increase in mEPSC frequency from P6 to P10 was almost completely blocked (Fig. 6 h), suggesting that synapse formation was partly prevented. After P10, no excess decrease in mEPSC frequency was found, indicating that synapse elimination was not enhanced. At all developmental time points, the PDE-Hr1 SynTAM slightly decreased the mEPSC amplitude, consistent with the shrunken synapse size observed by EM in cultured neurons (Fig. 6 i). The inactive PDE*-Hr1 SynTAM had no significant effect on either the mEPSC frequency or amplitude at any time of development (Fig. 6 i). These experiments strongly support the notion that a cAMP-dependent signaling pathway drives synapse formation not only in cultured neurons but also in vivo.

The changes in mEPSCs do not tell us whether all excitatory synapses onto a CA1 neuron are decreased or only a subset of synapses is affected. To address this question, we recorded evoked EPSCs elicited in CA1 neurons by stimulation of either Schaffer-collateral or entorhinal-CA1/temporoammonic-path axons, which form synapses on distinct dendritic domains of CA1 neurons (Anderson et al., 2017). AMPAR (α -amino-3-hydroxy-5-methyl-4-isoxazolepropionic acid receptor)-mediated synaptic responses were recorded at a holding potential of -70 mV, using input/output curves to control for differences in stimulation efficacy. NMDAR (*N*-methyl-D-aspartate receptor)-mediated responses were monitored in the same neurons by shifting the holding potential to +40 mV and were quantified at 50 ms after the stimulus artifact (Sando et al., 2019).

The PDE-Hr1 SynTAM equally suppressed the strength of Schaffer-collateral and entorhinal cortex synaptic inputs (~60% decrease), as manifested by a comparable decline in the slope of the AMPAR-EPSC input-output curves and of the amplitude of NMDAR-EPSCs (Fig. 7, a–d). In contrast, catalytically inactive PDE*-Homer1 had no significant effect on either AMPAR- or NMDAR-EPSCs at either synapse (Fig. 7, a–d). The phenotype induced by the PDE-Hr1 SynTAM is more robust than that obtained with *Lphn2* or *Lphn3* deletions in the same synapses (Anderson et al., 2017; Sando et al., 2019), likely because PDE-Hr1 targets both *Lphn2*- and *Lphn3*-dependent and *Lphn2*- and *Lphn3*-independent synapses. Altogether, these data support the hypothesis that localized postsynaptic cAMP signaling is essential for excitatory synapse formation in all dendritic domains of CA1 neurons.

Postsynaptic cAMP signaling is required for synaptic connectivity in the hippocampus

In the CA1 region of the adult hippocampus, ~100% of dendritic spine synapses are eliminated and reformed every few weeks, suggesting that synapse formation is continuously required for maintaining synaptic connectivity (Attardo et al., 2015; Pfeiffer et al., 2018; Wiegert et al., 2018). Thus, we used SynTAMs to examine the role of postsynaptic cAMP signaling in the maintenance of synaptic connectivity in CA1 region neurons of the

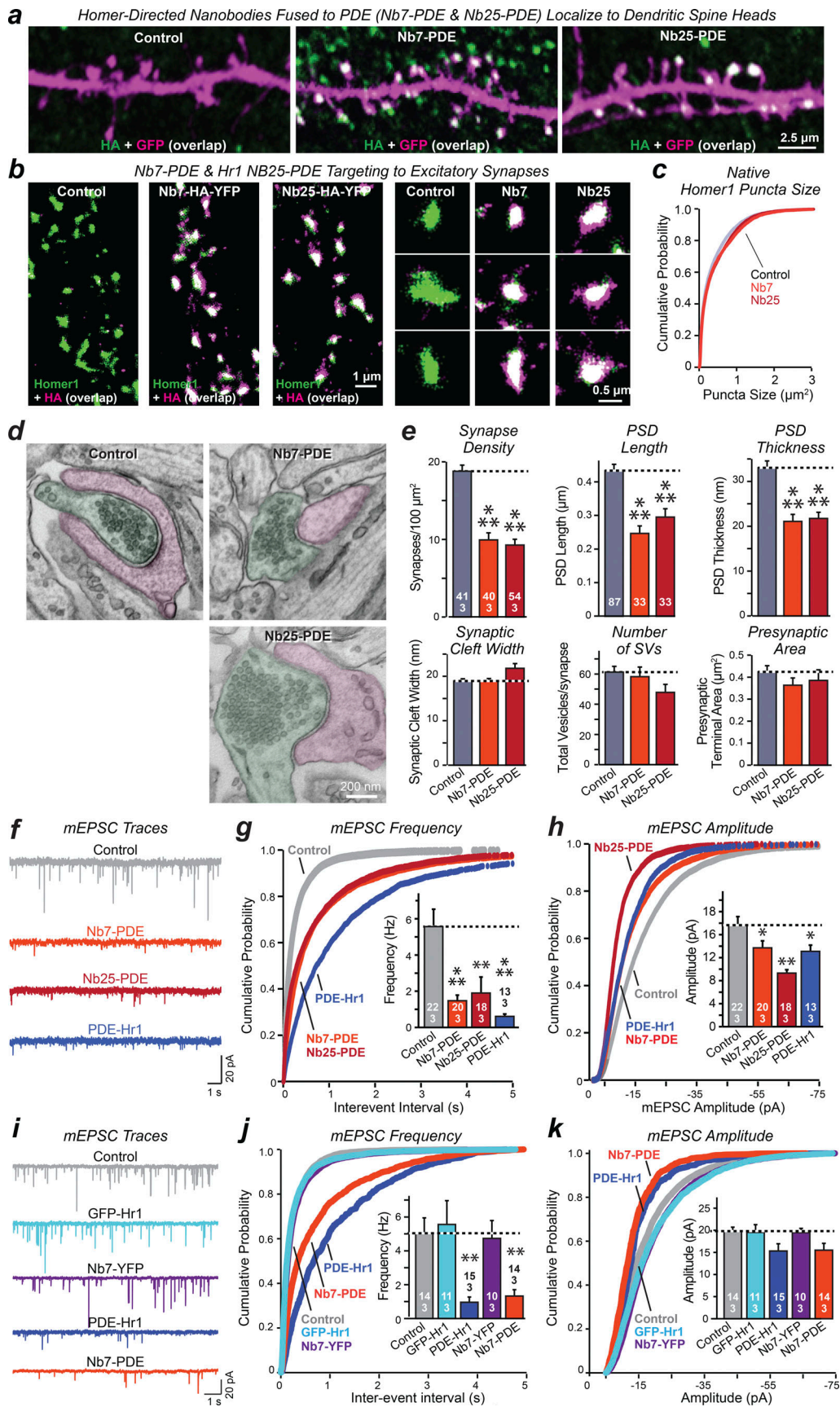


Figure 4. Nanobody-targeted SynTAMs impair excitatory synapse formation in hippocampal neurons. (a) Nb7-PDE and Nb25-PDE SynTAMs composed of anti-Homer1 nanobodies carrying a PDE7b cargo are specifically targeted to dendritic spine heads in cultured hippocampal neurons. Neurons infected with

lentiviruses encoding HA-tagged Nb7-PDE or Nb25-PDE were sparsely transfected with GFP to fill the cytosol and examined by ICC for HA. **(b and c)** Super-resolution two-color STORM imaging demonstrates that Homer1-targeting nanobodies (Nb7 and Nb25, both HA-tagged and fused to YFP) are specifically localized to postsynaptic densities (b) but do not alter the size of these densities (c). **(d and e)** EM analyses show that Nb7-PDE and Nb25-PDE SynTAMs reduce synapse numbers in cultured hippocampal neurons and alter the structure of the PSD of the remaining synapses. **(d)** Representative EM images (green, presynaptic terminals; pink, postsynaptic spines). **(e)** Summary graphs of the synapse density and the indicated structural parameters of synapses. **(f-h)** Local suppression of postsynaptic cAMP signaling by Nb7-PDE and Nb25-PDE SynTAMs impairs the frequency and amplitude of mEPSCs similar to PDE-Hr1. mEPSCs were monitored in neurons expressing Nb7-PDE, Nb25-PDE, and PDE-Hr1 in the presence of TTX. **(f)** Representative traces. **(g)** Cumulative probability plots of the mEPSC interevent interval (inset, summary graph of mEPSC frequency). **(h)** Cumulative probability plots of mEPSC amplitude (inset, summary graph of mEPSC amplitude). **(i-k)** Expression of the Homer1c-directed nanobody Nb7 or of Homer1c without fusion to PDE7b has no effect on mEPSCs in contrast to Nb7-PDE and PDE-Hr1 SynTAMs. **(i)** Representative traces. **(j)** Cumulative probability plots of the mEPSC interevent interval (inset, summary graph of mEPSC frequency). **(k)** Cumulative probability plots of the mEPSC amplitude (inset, summary graph of mEPSC amplitude). Data are means \pm SEM (numbers of analyzed cells/experiments or synapses are indicated in bars). Statistical significance was assessed by one-way ANOVA with post hoc Tukey tests for multiple comparisons (***, $P < 0.001$; **, $P < 0.01$; *, $P < 0.05$). For additional data, see Fig. S3. SV, synaptic vesicle; TTX, tetrodotoxin.

adult hippocampus using rabies virus tracing (Callaway, 2008). We employed a sparse rabies virus-tracing strategy to assess the abundance of synaptic inputs onto hippocampal CA1 neurons expressing PDE-Hr1 and PDE*-Hr1 SynTAMs (Fig. 8, a and b; and Fig. S5, i-k). CA1 pyramidal neurons expressing catalytically active PDE-Hr1 displayed a striking decrease ($\sim 90\%$) in Schaffer-collateral and entorhinal-CA1/temporoammonic-path inputs (Fig. 8, c-e; and Fig. S5, i-k). Inputs from the ipsilateral and contralateral CA3 regions were equally suppressed. Catalytically inactive PDE*-Hr1, however, had no effect. Furthermore, PDE7b expressed alone also did not change synaptic connectivity, suggesting that local postsynaptic suppression of cAMP is required to impair synaptic connectivity (Fig. 8, c-e). These results indicate that compartmentalized postsynaptic cAMP signaling is critical for the establishment and maintenance of synaptic connectivity in hippocampal circuits.

Discussion

The intracellular signals that regulate assembly of pre- and postsynaptic specializations during synapse formation are largely unknown (Südhof, 2021). Previous studies suggested a possible role of postsynaptic cAMP signaling in inducing synapse formation (Kwon and Sabatini, 2011), consistent with the function of latrophilins as G protein coupled receptors that stimulate synapse formation and induce cAMP synthesis (Sando and Südhof, 2021), but no tools were available to test a specific role for cAMP in synapse formation. Although reliable pharmacological approaches exist for controlling cAMP signaling in cells, these approaches invariably alter cAMP signaling in an entire cell. Thus, we designed new molecular tools referred to as SynTAMs that enable spatially restricted suppression of cAMP signaling in developing postsynaptic specializations. SynTAMs deliver an active “cargo” to developing excitatory postsynaptic specializations and can in principle be applied to any signaling pathway. We constructed two types of SynTAMs that employ different mechanisms for targeting a cargo to postsynaptic specializations. First, we fused PDE7b or PKI to Homer1c, a PSD scaffolding protein (Xiao et al., 2000; Kennedy, 2000; Worley et al., 2007). We demonstrated that the resulting SynTAMs (PDE-Hr1 and PKI-Hr1) are concentrated in excitatory PSDs (Fig. 1 b and Fig. S1). Second, we fused PDE7b to nanobodies that recognize Homer1 when they are expressed as intrabodies in neurons (Nb7 and Nb25; see Dong et al., 2019). Again, the

resulting SynTAMs (Nb7-PDE and Nb25-PDE) were exclusively targeted to excitatory PSDs (Fig. 4, a-c; and Fig. S3). These tools enabled us to selectively suppress cAMP signaling in developing postsynaptic specializations.

Our results show that if cAMP signaling is suppressed in developing postsynaptic specializations using SynTAMs before mature synaptic connections are established, formation of most functional synapses is blocked, as analyzed both in cultured neurons (Fig. 1, Fig. 2, Fig. 3, and Fig. 4) and in vivo (Fig. 5, Fig. 6, and Fig. 7). Moreover, the residual synapses that are still assembled are smaller and weaker (Fig. 1, i and j; Fig. 2; Fig. 6; and Fig. S2, c and d). Suppressing cAMP levels at other subcellular locations of neurons had no effect on developing excitatory synapses (Fig. 3). These findings suggest that cAMP, a universal second messenger involved in multifarious cellular functions, unexpectedly also serves as a specific local signal that drives synapse assembly. Moreover, in the adult hippocampus in which synapses continuously turn over with a half-life of less than a week (Attardo et al., 2015; Pfeiffer et al., 2018), suppression of cAMP signaling also severely impaired synaptic connectivity (Fig. 8).

Our study also has limitations that need to be addressed in the future. We did not assess if cAMP levels are increased locally during synapse formation. At present no methods are available to identify nascent synapses, and imaging of cAMP only visualizes relative phasic changes, not tonic local signaling that we implicate in synapse formation. We also did not show that cAMP generation by itself produces synapses. However, cAMP alone is unlikely to induce synapse formation because cAMP is a universal messenger that regulates multifarious cellular processes in a spatially compartmentalized manner (Argyrousi et al., 2020; Averaimo and Nicol, 2014; Zaccolo et al., 2021; Johnstone et al., 2018). cAMP has little inherent specificity, which is conferred by the spatial context. cAMP acts during synapse formation in a defined molecular environment that enables cAMP-dependent activation of particular downstream effectors, most likely PKA substrates. This molecular context may be produced in nascent synaptic junctions by multiple parallel trans-cellular signals but would be absent if we simply stimulated cAMP production in a dendrite.

Not surprisingly, our results prompt multiple new questions. Is it possible that cAMP acts as a synapse maintenance signal instead of a synapse assembly signal? The experiments measuring mEPSCs as a function of development show that

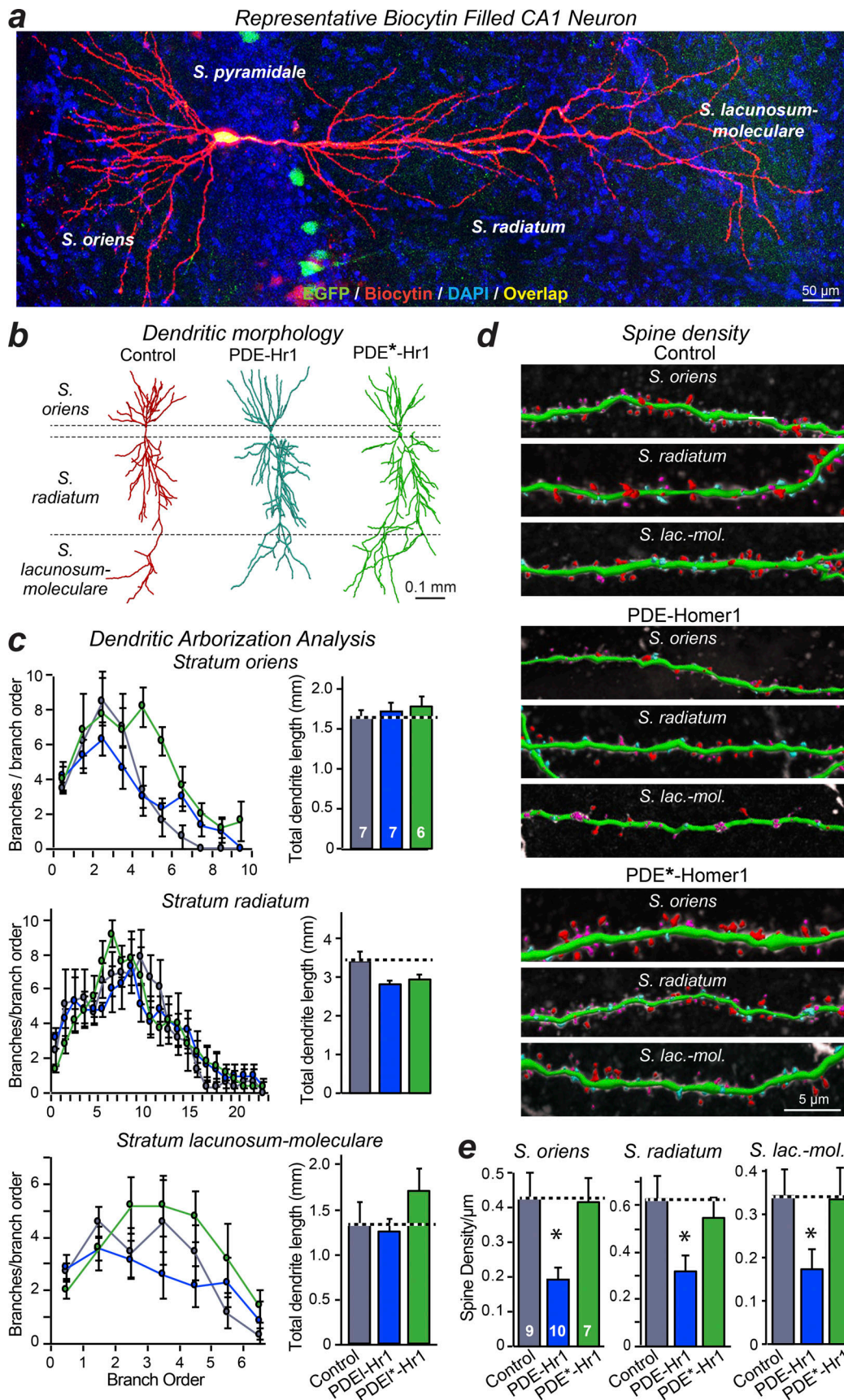


Figure 5. **SYNTAM-mediated in vivo cAMP suppression in developing excitatory postsynaptic specializations of CA1 neurons reduces spine density without affecting dendritic arborization.** (a–e) For all experiments, the CA1 region of newborn mice was sparsely infected with lentiviruses coexpressing

GFP and the indicated proteins and analyzed at P21–25. **(a)** Representative image of a CA1 neuron that was infected in vivo with lentiviruses encoding PDE-Hr1 coexpressing EGFP and filled in acute slices with biocytin during whole-cell voltage-clamp recordings. Dendritic arbors and spines of biocytin-filled neurons were reconstructed using NeuroLucida 360. **(b and c)** Suppression of postsynaptic cAMP levels in vivo using PDE-Hr1 has no effect on dendritic development. **(b)** Representative reconstructions of dendritic arbors from reconstructed control neurons or neurons expressing PDE-Hr1 or catalytically inactive PDE*-Hr1. **(c)** Dendritic arborization measurements from representative CA1 pyramidal neuron reconstructions (graphs show numbers of branches per branch order [left] or total dendrite length [right] for the *S. oriens*, *S. radiatum*, and *S. lacunosum-moleculare*). **(d and e)** PDE-Hr1 decreases the dendritic spine density equally in the *S. oriens*, *S. radiatum*, and *S. lacunosum-moleculare* (*S. lac.-mol.*) of the CA1 region, whereas inactive PDE*-Hr1 has no effect. **(d)** Representative dendrites (green = dendritic shafts; red, cyan, and purple = mushroom, stubby, and thin spines, respectively). **(e)** Summary graphs of the spine density in the indicated dendritic domains. Data in c and e are means \pm SEM (numbers of cells/experiments are indicated in bars). Statistical significance was assessed by one-way ANOVA or two-way ANOVA with post hoc Tukey tests for multiple comparisons (*, $P < 0.05$). For additional data, see Fig. S4.

suppression of cAMP signaling prevents the initial establishment of functional synapses (Fig. 2 and Fig. 6). In cultured control neurons, mEPSCs are sparse at DIV6 and become more frequent at DIV8, but PDE-Hr1 completely blocked their increase at DIV8 (Fig. 2 k). In vivo, PDE-Hr1 suppressed most initial synapse formation as monitored by mEPSCs at P6, the first time point measured, and prevented the subsequent excess synapse formation (Fig. 6 h). If cAMP was a survival signal for synapses, it thus would be required for maintaining the survival of a synapse immediately after it was formed. Such a survival function would arguably be more part of synapse formation than synapse maintenance. In fact, it seems likely that cell–surface interactions first induce a nascent synaptic junction, that this induction results in increased postsynaptic cAMP levels, and that the cAMP signal then organizes the synaptic specializations. As a result, cAMP would not be required for the initial emergence of a nascent synaptic junction, but for its development into a functional synapse. According to this model, cAMP is not a survival signal but an assembly signal.

Another question regards the mechanisms that compartmentalize cAMP signaling at the synapse. Likely PKA anchoring proteins (AKAPs) that are abundant in the postsynaptic compartment are involved (Nair et al., 2013; Patriarchi et al., 2018; Sanderson et al., 2018), but the specific molecular pathways remain to be explored. Furthermore, how general is the role of localized cAMP signaling in synapse formation? In our experiments, this role is specific for excitatory synapses because Homer1c targeting is restricted to excitatory synapses, but we found that at least in CA1 neurons, both Schaffer-collateral and entorhinal-CA1 synapse assembly required cAMP signaling, suggesting a general role. An additional question concerns the persistence of some excitatory synapses after SynTAM-mediated suppression of cAMP signaling. It is possible that a subset of synapses may use other signal transduction pathways or that the suppression of cAMP signaling by SynTAMs is not equally effective in all synapses. Finally, what is the mechanism by which cAMP promotes synapse formation? cAMP probably acts by activating PKA, since targeting of PKI to postsynaptic specializations also impaired synapse formation (Fig. 1, c and d; Fig. 2 g–i; and Fig. 6 c), but the substrates of PKA in synapse formation and their functions remain unknown. These questions are fertile ground for future studies.

In summary, we designed SynTAM tools that enable suppression of local cAMP signaling in nascent postsynaptic specializations, and we demonstrated using SynTAMs that local postsynaptic cAMP signaling is a key driver in synapse

formation. This finding provides a new perspective that at the same time simplifies and expands our present understanding of synapse formation.

Materials and methods

Resources

Resources are listed in Table 1.

Mice

Overexpression studies were conducted in primary hippocampal cultures from CD1 mice or C57BL/6 mice in vivo. Mice were weaned at 18–21 d of age and housed in groups of 2–5 on a 12-h light/dark cycle with food and water ad libitum. At Stanford Animal Housing Facility, all procedures conformed to National Institutes of Health Guidelines for the Care and Use of Laboratory Mice and were approved by the Stanford University Administrative Panel on Laboratory Animal Care.

Plasmids

For phosphodiesterase PDE7b expression experiments, human PDE7b cDNA was used, with HEK293T cell expression mediated by pCMV5 or pcDNA3 vectors and expression in cultured neurons or in vivo mediated by lentiviruses using the rat synapsin-1 promoter or adeno-associated viruses (AAVs) using the CAG promoter. Considering many PDEs hydrolyze both cAMP and cyclic GMP, PDE7b was used due to its high affinity and selectivity for cAMP. The following sequences were used for targeting PDE7b to specific subcellular compartments: PDE-Hr1: PDE7b was fused to the N-terminus of rat Homer1c with a 6× glycine linker; PDE*-Hr1: same as PDE-Hr1 except that the PDE7b sequence contained two point mutations in the metal-binding site (H694A, D695A) that block PDE catalytic activity; ER-PDE: encodes PDE7b with an N-terminal calreticulin signal peptide (MLLSVPLLLGLLGLAAA) and a C-terminal KDEL sequence that prevents ER export; mitoPDE7b: encodes PDE7b with an N-terminal mitochondrial targeting sequence from COX8 (MSVLTPLLLRGLTGSARRLPVPRAKIHSLGDPVATM); NLS-PDE7b: encodes PDE7b with an N-terminal nuclear localization signal from nucleoplasmin (MVKRPAATKKAGQAKKKK); Pink Flamindo cAMP Reporter: a gift from Tetsuya Kitaguchi (Waseda University, Tokyo, Japan; Addgene plasmid #102356); and Rabies Complementing AAVs: AAV CAG FLEX TVA-mCherry and AAV CAG FLEX RG, gifts from Liqun Luo (Howard Hughes Medical Institute, Stanford University, Stanford, CA; Addgene #48332 and #48333).

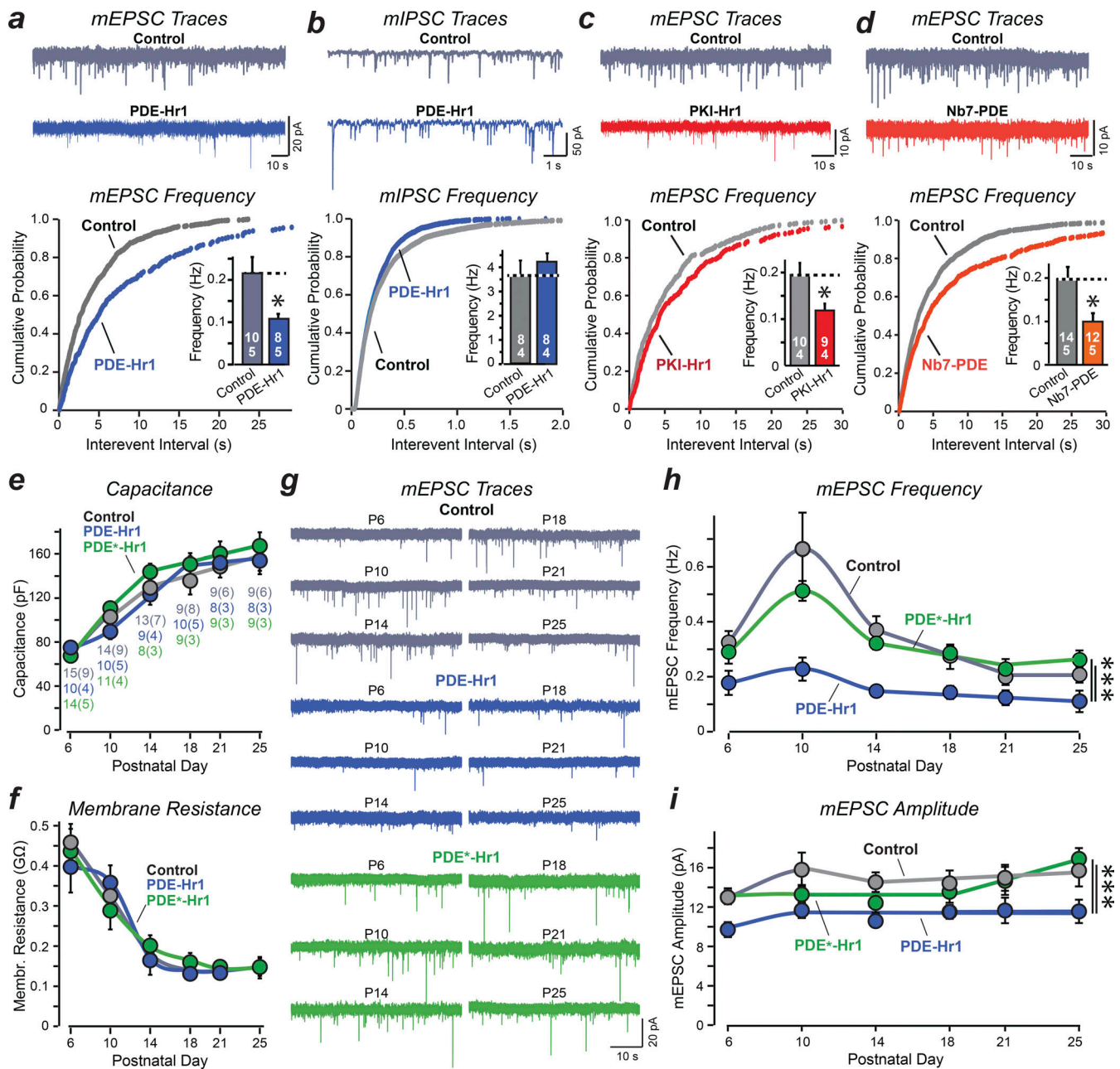


Figure 6. SynTAM-mediated in vivo suppression of postsynaptic cAMP levels in developing postsynaptic densities impairs formation of functional excitatory synapses. (a) Suppression of postsynaptic cAMP levels using PDE-Hr1 decreases mEPSC frequency in CA1 pyramidal neurons (top: representative mEPSC traces; bottom: cumulative probability plots of mEPSC interevent interval [inset, summary graph of mEPSC frequency]). Control conditions were cells from slices in the opposite uninfected hemisphere. (b) PDE-Hr1 does not affect mIPSCs in CA1 pyramidal neurons. Same as a, except that mIPSCs were monitored. (c) PKI-Hr1, which inhibits postsynaptic PKA, decreases mEPSC frequency and amplitude in CA1 pyramidal neurons. Same as a, but for PKI-Hr1. (d) Nanobody-mediated suppression of postsynaptic cAMP signaling in CA1 pyramidal neurons in vivo using Nb7-PDE decreases mEPSC frequency. Same as a, except for Nb7-PDE. (e and f) Capacitance (e) and membrane (Membr.) resistance measurements (f) of hippocampal neurons expressing PDE-Hr1 or PDE*-Hr1 in comparison to noninfected control neurons as a function of postnatal development reveal a typical capacitance increase and membrane resistance decrease as the neurons mature, without significant differences between control neurons and neurons expressing either PDE-Hr1 or PDE*-Hr1. (g–i) Suppression of postsynaptic cAMP levels impairs the initial formation of functional synapses as revealed by mEPSC measurements as a function of development. mEPSCs were recorded at the indicated times following P0 lentiviral infections in vivo. Note that postsynaptic cAMP depletion nearly abolishes the excess synapse formation and elimination at P6–P18. (g) Representative mEPSC traces. (h) Summary graph of mEPSC frequencies. (i) Summary graph of mEPSC amplitude. Data are means \pm SEM (numbers of cells/experiments are indicated in bars). Statistical significance was assessed by a two-tailed t test, one-way or two-way ANOVA with post hoc Tukey tests for multiple comparisons (***, $P < 0.001$; *, $P < 0.05$). For additional data, see Fig. S5.

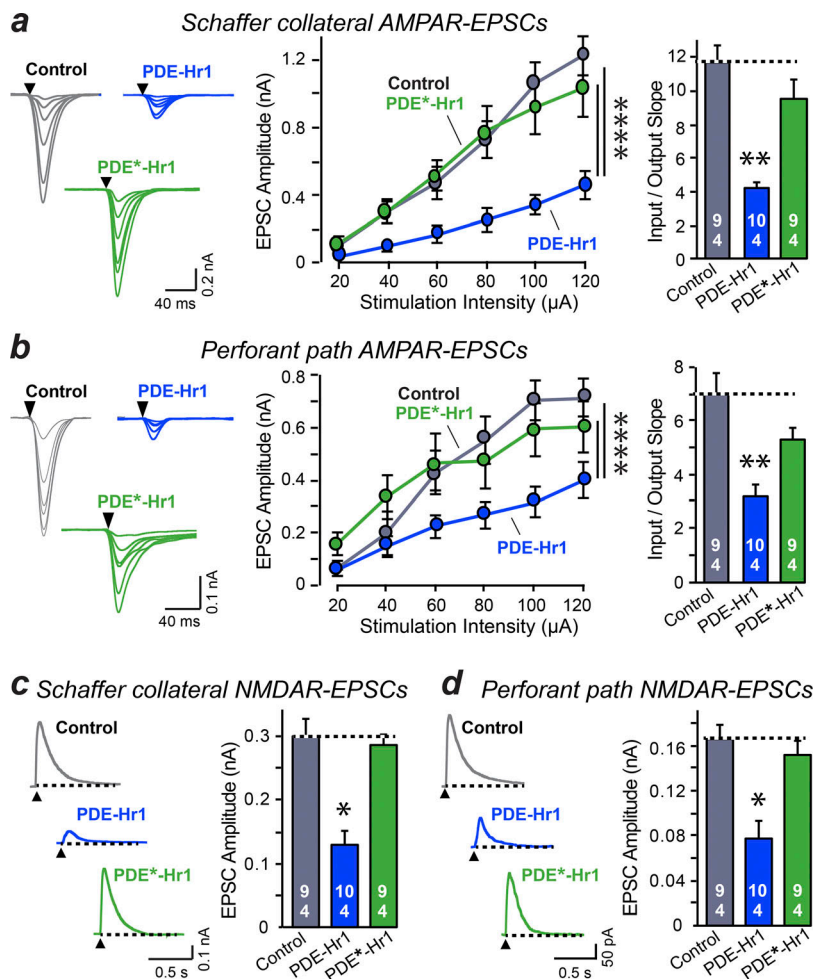


Figure 7. SynTAM-mediated in vivo suppression of postsynaptic cAMP signaling impairs excitatory synaptic connections. (a and b) Suppression of postsynaptic cAMP levels in vivo using expression of PDE-Hr1 but not of catalytically inactive PDE*-Hr1 reduces the amplitude of synaptic responses evoked by stimulation of Schaffer-collateral synapses. AMPAR-EPSCs were monitored via input/output curves to control for stimulation intensity at a -70 mV holding potential, while NMDA-receptors were analyzed separately in the same neurons at a $+40$ mV holding potential. (a) Left: representative Schaffer-collateral AMPAR-EPSC traces; middle: summary input-output plots of recordings at -70 mV holding potential; right: summary graph of AMPAR-EPSC average input/output slope. (b) Same as a, but analyzed for entorhinal-CA1/temporoammonic-path synapses. ****, $P < 0.0001$. (c) Representative Schaffer collateral NMDAR-EPSC traces. (c) Left: representative NMDAR-EPSC traces; right: summary graph of the average NMDAR-EPSC amplitude monitored at a $+40$ mV holding potential in the same cells as in a. (d) Same as c, but analyzed for entorhinal-CA1 path synapses. Data are means \pm SEM (numbers of cells/experiments are indicated in bars). Statistical significance was assessed by a two-tailed t test, one-way or two-way ANOVA with post hoc Tukey tests for multiple comparisons (**, $P < 0.01$; *, $P < 0.05$). Arrowheads denote site of stimulation artifact.

Antibodies

The following antibodies were used at the indicated concentrations (immunohistochemistry [IHC]; ICC; and immunoblot [IB]): anti-HA mouse (Covance; Cat# MMS101R; 1:500 IHC; 1:1,000 ICC; 1:2,000 IB), anti-HA rabbit (Cell Signaling Technologies; Cat# 3724; 1:2,000 ICC; 1:1,000 IHC), anti- β -actin mouse (Sigma; Cat# A1978; 1:10,000 IB), anti-Map2 chicken (Encor; Cat# CPCA MAP2; 1:2,000 ICC), anti-Map2 mouse (Sigma; Cat# M1406; 1:1,000 ICC), anti-PSD-95 mouse (Synaptic Systems; Cat# 124011; 1:2,000 ICC), anti-vGLUT1 guinea pig (Millipore; Cat# AB5905; 1:2,000 ICC), Streptavidin Alexa Fluor 488 (Thermo Fisher Scientific; Cat# S32354; 1:1,000 IHC), Streptavidin Alexa Fluor 555 (Invitrogen; Cat# S21381; 1:1,000 IHC), Alexa Fluor 546 Phalloidin (Invitrogen; Cat# A22283; 1:500 ICC), anti-Homer1 rabbit (Millipore; Cat# ABN37; 1:1,000 ICC), anti-Homer1 rabbit (Synaptic Systems; Cat# 160003; 1:2,000 ICC), anti-gephyrin mouse (Synaptic Systems; Cat# 147111; 1:2,000 ICC), and fluorescently conjugated goat secondary antibodies from Life Technologies.

Cultured hippocampal neurons

Hippocampi were dissected from P0 CD-1 mice, and cells were dissociated by papain (Worthington; Cat# LS003127) digestion for 20 min at 37°C , filtered through a $70\text{-}\mu\text{m}$ cell strainer (Falcon; Cat# 352350), and plated on Matrigel (Corning; Cat# 356235)-

coated 0-thickness glass coverslips (Assistent; Cat# 01105209) in 24-well plates. Plating media contained 5% fetal bovine serum (Atlanta), B27 (Gibco; Cat# 17504044), 0.4% glucose (Sigma), and 2 mM glutamine (Gibco; Cat# 25030164) in $1\times$ MEM (Gibco; Cat# 51200038). Culture medium was exchanged to growth medium 24 h later (1 DIV), which contained 5% fetal bovine serum (Atlanta), B27 (Gibco), and 2 mM glutamine (Gibco) in Neurobasal A (Gibco; Cat# 10888022). Cytosine arabinofuranoside (Sigma; Cat# C6645) was added at a final concentration of $4\ \mu\text{M}$ on 3 DIV in a 50% growth media exchange, and neurons were analyzed 14–16 DIV.

Virus production

For production of lentiviruses, the lentiviral expression shuttle vector and three helper plasmids (pRSV-REV, pMDLg/pRRE, and vesicular stomatitis virus G protein) were cotransfected into low-passage (<10 passages) HEK293T cells (American Type Culture Collection; CRL-11268) at $5\ \mu\text{g}$ of each plasmid per $25\ \text{cm}^2$ culture area, respectively. Control conditions aside from GFP- ΔCre or GFP-infected controls were lentivirus produced with empty shuttle vector. Transfections were performed using the calcium-phosphate method with 2.5 M CaCl_2 and $2\times$ Hanks buffered saline, pH 7.05 (274 mM NaCl, 10 mM KCl, 1.5 mM $\text{Na}_2\text{HPO}_4\ 7\ \text{H}_2\text{O}$ [dibasic], 12 mM dextrose, and 42 mM HEPES). Medium with viruses was collected at 48 h after transfection, centrifuged at $5,000\times g$ for 5 min to pellet cellular debris, filtered

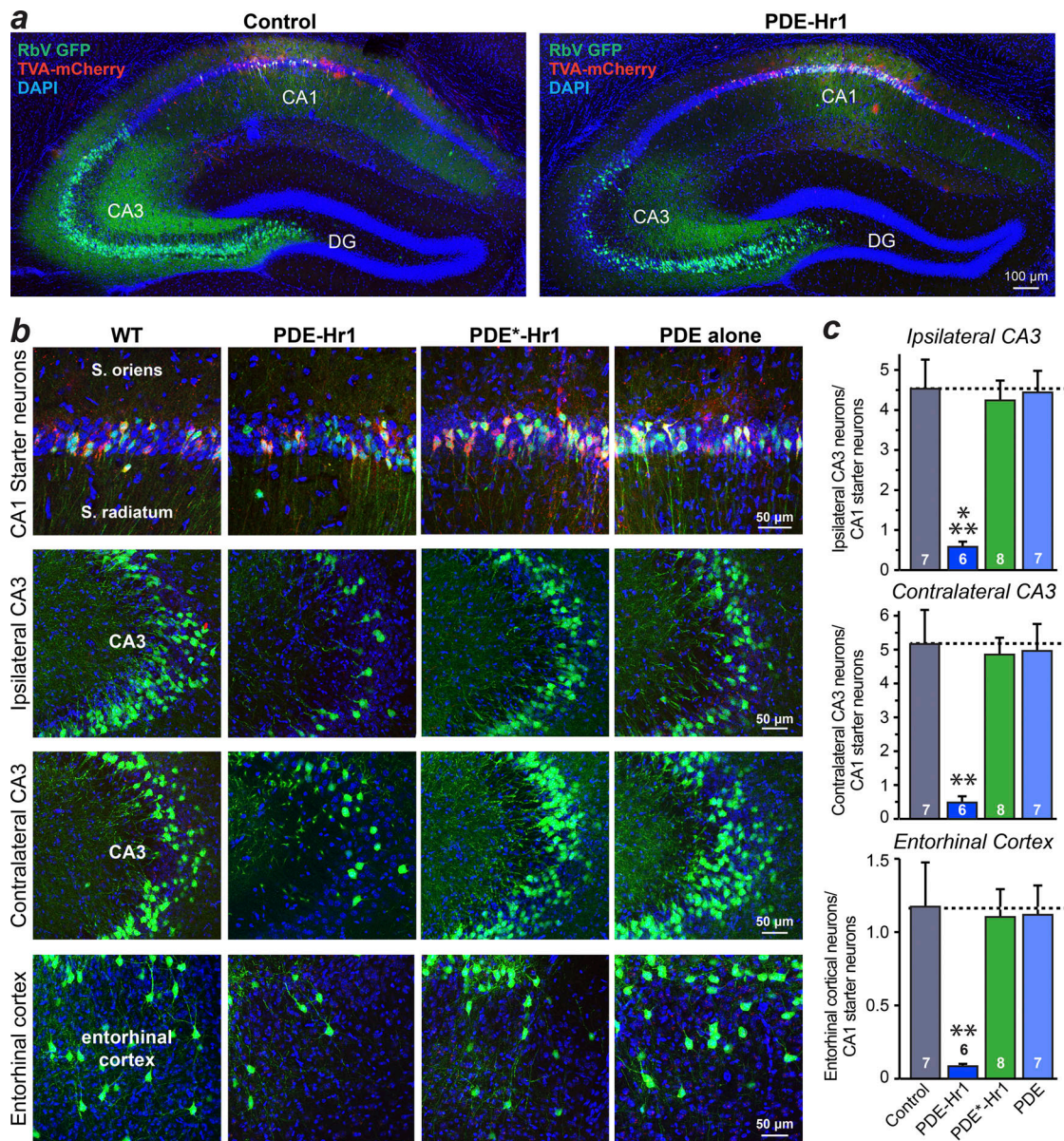


Figure 8. **SynTAM-mediated in vivo suppression of postsynaptic cAMP severely reduces the synaptic connectivity of adult hippocampal CA1 region neurons.** (a) Representative overviews of hippocampi from retrograde rabies virus-tracing experiments. Starter cells in the CA1 region express both mCherry and EGFP, while presynaptic CA1 and CA3 neurons express only EGFP. (b) Representative images of CA1 starter cells (top) and of presynaptic input neurons in the ipsilateral CA3 region, the contralateral CA3 region, and the ipsilateral entorhinal cortex (bottom panels). (c) Quantifications of EGFP-positive cells in the indicated presynaptic input regions normalized for the number of CA1-region starter cells. PDE-Hr1 expression in CA1-region neurons decreased synaptic inputs from the ipsi-/contralateral CA3 regions and ipsilateral entorhinal cortex, whereas catalytically inactive PDE*-Hr1 and cytoplasmic PDE had no significant effect. Data are means \pm SEM (numbers of mice are indicated in bars). Statistical significance was assessed by one-way ANOVA with post hoc Tukey tests for multiple comparisons (**, $P < 0.01$; ***, $P < 0.001$, comparing PDE-Hr1 with all other conditions). For additional data, see Fig. S5. DG, dentate gyrus; RbV, rabies virus; TVA, EnvA receptor.

(0.45- μ m pore size), and added directly to primary cultures for in vitro experiments. For in vivo injections, virus was produced at the Janelia Farm Virus Core Facility where infectious titer was determined, and equal numbers of viral particles were injected for each experiment.

For production of AAVs expressing PDE7b or PDE7b fusions, five 10-cm² plates of HEK293T cells at 90% confluency were transfected via the calcium phosphate method. For transfections, 100 μ g of each plasmid (pHelper, pDJ, and AAV shuttle

plasmid) was mixed to a volume of 6.75 ml dH₂O, and 0.75 ml of 2.5 M CaCl₂ was added. The DNA/CaCl₂ mixture was added dropwise to 7.5 ml 2 \times HBS, pH 7.05 (274 mM NaCl, 10 mM KCl, 1.5 mM Na₂HPO₄, 7 H₂O [dibasic], 12 mM dextrose, and 42 mM Hepes) while vortexing gently. The DNA/CaPO₄ mixture was incubated at room temperature for 20 min, and then 3 ml was added dropwise to each plate. Cells were washed 1 \times with pre-warmed PBS 24 h after transfection, and medium was replaced with fresh complete DMEM (DMEM + 10% FBS). Cells were

Table 1. **Resources table**

Reagent or resource	Source	Identifier
Antibodies		
Anti-HA mouse	Covance/BioLegend	MMS101R
Anti-HA rabbit	Cell Signaling Technologies	3724
Anti- β -Actin mouse	Sigma	A1978
Anti-MAP2 chicken	Encor	CPCA MAP2
Anti-MAP2 mouse	Sigma	M1406
Anti-PSD-95 mouse	Synaptic Systems	124011
Anti-vGLUT1 guinea pig	Millipore	AB5905
Anti-Homer1 rabbit	Synaptic Systems	160003
Anti-Homer1 rabbit	Millipore	ABN37
Anti-gephyrin mouse	Synaptic Systems	147111
Goat anti-mouse Alexa Fluor 488	Thermo Fisher Scientific	A11001
Goat anti-mouse Alexa Fluor 546	Thermo Fisher Scientific	A11003
Goat anti-mouse Alexa Fluor 647	Thermo Fisher Scientific	A21236
Goat anti-rabbit Alexa Fluor 488	Thermo Fisher Scientific	A11034
Goat anti-rabbit Alexa Fluor 546	Thermo Fisher Scientific	A11010
Goat anti-rabbit Alexa Fluor 647	Thermo Fisher Scientific	A21245
Goat anti-chicken Alexa Fluor 647	Thermo Fisher Scientific	A21449
Goat anti-guinea pig Alexa Fluor 647	Thermo Fisher Scientific	A21450
Anti-mouse CF568	Biotium	20105-1mg
Donkey anti-mouse 800CW	Licor	92632212
Donkey anti-rabbit 800CW	Licor	92632213
Bacterial and virus strains		
DH10 β	Thermo Fisher Scientific	18297010
Lentiviral VSVG	Commonly available plasmid	N/A
Adeno-associated virus DJ capsid	Commonly available plasmid	N/A
Biological samples		
Primary hippocampal cultures	CD1 mice from Charles River Laboratories	N/A
Hippocampal brain tissue	C57/Bl6 mice	N/A
Chemicals, peptides, and recombinant proteins		
Streptavidin Alexa Fluor 488	Thermo Fisher Scientific	S32354
Streptavidin Alexa Fluor 555	Invitrogen	S21381
Alexa Fluor 546 phalloidin	Invitrogen	A22283
Cytosine arabinofuranoside	Sigma	C6645
QX-314	Tocris	1014
Picrotoxin	Tocris	1128
Tetrodotoxin	Tocris	1069
D-AP5	Tocris	0106
CNQX	Tocris	1045
Benzonase nuclease	Sigma	E1014
PFA	Electron Microscopy Science	15714
2,2,2-tribromoethanol	Sigma	T48402
Biocytin	Sigma	B4261
Glucose oxidase	Sigma	G2133

Table 1. **Resources table (Continued)**

Reagent or resource	Source	Identifier
Catalase	Sigma	C40
DAPI	Roche	10236276001
Critical commercial assays		
N/A		
Deposited data		
All raw numerical data within figures are submitted with manuscript		
Experimental models: cell lines		
HEK293T	ATCC	CRL-11268
Experimental models: organisms/strains		
CD-1	Charles River	N/A
C57/BL6	The Jackson Laboratory	000664
Oligonucleotides		
Various cloning primers	IDT	N/A
Recombinant DNA		
Pink Flamingo cAMP reporter	Addgene	102356
pAAV CAG FLEX TVA-mCherry	Addgene	48332
pAAV CAG FLEX RG	Addgene	48333
Lenti HA-PDE7b	This paper	N/A
Lenti Syn PDE7b-Hr1	This paper	N/A
Lenti EF1a PDE7b-Hr1	This paper	N/A
Lenti Syn PDE7b*-Hr1	This paper	N/A
Lenti Syn ER-PDE7b	This paper	N/A
Lenti Syn mitoPDE7b	This paper	N/A
Lenti Syn NLS-PDE7b	This paper	N/A
Lenti EF1a PKI-Hr1	This paper	N/A
Lenti Syn Hr1 Nanobody7-PDE7b	This paper	N/A
Lenti Syn Hr1 Nanobody25-PDE7b	This paper	N/A
Lenti Syn Hr1 Nanobody7-YFP	Dong et al., 2019 ; ELife	N/A
Lenti Syn Hr1 Nanobody25-YFP	Dong et al., 2019 ; ELife	N/A
Lenti Syn HA-Homer1	This paper	N/A
Lenti Syn GFP p2a PDE7b-Hr1	This paper	N/A
Lenti Syn GFP p2a PDE7b*-Hr1	This paper	N/A
Lenti EF1a PKI-Hr1 p2a tdTomato	This paper	N/A
Lenti EF1a Hr1 Nanobody7-PDE7b p2a tdTomato	This paper	N/A
pAAV CAG PDE7b-Hr1	This paper	N/A
pAAV CAG PDE7b*-Hr1	This paper	N/A
pAAV CAG PDE7b	This paper	N/A
Lenti Syn GFP-Homer1	This paper	N/A
Software		
SnapGene	GSL Biotech	
pClamp10	Molecular Devices	
Clampfit 10	Molecular Devices	
NIS-Elements AR	Nikon	
ImageJ	National Institutes of Health	

Table 1. Resources table (Continued)

Reagent or resource	Source	Identifier
Adobe Photoshop	Adobe	
Adobe Illustrator	Adobe	
GraphPad Prism 8.0	GraphPad	
NeuroLucida360	MBF Bioscience	
Vutara SRX	Bruker Vutara	
NeuronStudio	CNIC	
Other		
N/A		

ATCC, American Type Culture Collection; N/A, not applicable; pAAV - plasmid adeno-associated virus; VSVG, vesicular stomatitis virus.

harvested 72 h after transfection by 1× wash with PBS followed by addition of dissociation buffer (PBS/10 mM EDTA). A cell scraper was used to facilitate detachment, and cell suspensions were subsequently centrifuged at 1,500×g for 15 min at 4°C. Cell pellets were resuspended in 4 ml freezing buffer (150 mM NaCl, 20 mM Tris, pH 8.0, and 2 mM MgCl₂), snap-frozen in 70% ethanol/dry ice for 15 min, and rapidly thawed at 37°C. After three subsequent rounds of freeze/thaws, the cell suspension was incubated in 50 U/ml Benzonase nuclease (Sigma; Cat# E1014) for 30 min at 37°C. Samples were subsequently centrifuged at 3,000×g for 30 min. Supernatant was applied to the surface of an iodixanol gradient (15%, 25%, 40%, and 60%) and ultracentrifuged at 80,000×g for 2 h at 4°C. The 40% iodixanol gradient was harvested, added to 10 ml PBS/1 mM MgCl₂, and concentrated in centricon concentrating tubes (100,000 MWCO; Millipore; UFC0910024), which were preequilibrated with PBS/MgCl₂. Samples were concentrated to 100 µl, aliquoted, and stored at -80°C.

Sparse transfections of cultured neurons

Neuronal transfection was performed 7 d after plating using a calcium phosphate method to achieve sparse delivery of plasmids to isolated neurons that were identified by GFP expression. A DNA/calcium phosphate precipitate was prepared by mixing the following (per well, 24-well plate): 1 µg of DNA, 2 µl of 2 M CaCl₂, and dH₂O to a volume of 15 µl. DNA mixture was added dropwise under constant, low-powered vortex to an equal volume of 2× Hepes-buffered saline (274 mM NaCl, 10 mM KCl, 1.4 mM Na₂HPO₄, 15 mM D-glucose, and 42 mM Hepes, pH 7.05). The precipitate was allowed to form for 15 min at room temperature before addition to the cultures. Cultured neurons were placed in serum-free MEM (0.5 ml per well) supplemented with the NMDA receptor blocker AP-5 (50 µM; Tocris; Cat# 0106) and 10 mM MgCl₂. The original conditioned medium was saved and stored at 37°C. 30 µl of the DNA/calcium phosphate precipitate was added dropwise to each well. Dishes were returned to 5% CO₂ incubator at 37°C for 30 min. The incubation was stopped by washing the cells twice with 1 ml per well of prewarmed MEM. The conditioned medium was subsequently added back to each well, and the cells were returned to the CO₂ incubator and analyzed at 14 DIV.

ICC

Cells were washed briefly once with PBS, fixed with 4% PFA (Electron Microscopy Science; Cat# 15714)/4% sucrose/PBS for 20 min at 4°C, washed 3 × 5 min in PBS, and permeabilized in 0.2% Triton X-100/PBS for 5 min at room temperature. Cells were subsequently placed in blocking buffer (4% BSA; Sigma; Cat# 10735086001/3% goat serum; Sigma; Cat# G9023/PBS) for 1 h, incubated with diluted primary antibodies in blocking buffer overnight at 4°C, washed 3 × 5 min in PBS, incubated with diluted fluorescently conjugated secondary antibodies in blocking buffer for 1 h, counterstained with DAPI in PBS for 15 min at room temperature (Sigma; Cat# 10236276001), washed 3× in PBS, and mounted on UltraClear microscope slides (Denville Scientific; Cat# M1021) using Fluoromount-G (Southern Biotech; Cat# 0100-01).

IB

Cells were briefly washed once with PBS, and samples were collected in sample buffer containing 312.5 mM Tris-HCl, pH 6.8, 10% SDS, 50% glycerol, 12.5% 2-mercaptoethanol, bromophenol blue, and protease inhibitors (Sigma; Cat# 5056489001) and run on SDS-PAGE gels (12% PAGE gels for HA-PDE and β-actin IBs) at 30 mA/gel constant current. The Precision Plus Protein Dual Color Protein Standard (Bio-Rad; Cat# 1610374) was used as a protein molecular weight ladder. Protein was transferred onto nitrocellulose transfer membrane in transfer buffer (25.1 mM Tris, 192 mM glycine, and 20% methanol) at 200 mA constant current for 2 h at 4°C. Membranes were blocked in 5% nonfat dry milk/TBS with Tween-20 (TBST; 20 mM Tris-HCl, pH 7.4, 150 mM NaCl, and 0.05% Tween-20) for 1 h at room temperature, incubated in primary antibodies diluted into 5% milk/TBST overnight at 4°C, washed 3 × 5 min in TBST, incubated in corresponding secondary antibodies (Licor IRDye 800CW donkey anti-mouse; Cat# 92632212; IRDye 800CW donkey anti-rabbit Cat# 92632213) diluted into TBST, washed 5 × 5 min in TBST, and imaged on a Licor Odyssey system.

Electrophysiology of cultured neurons

For whole-cell patch-clamp experiments, the patch pipettes were pulled from borosilicate glass capillary tubes (World

Precision Instruments; Cat# TW150-4) using a PC-10 pipette puller (Narishige). The resistance of pipettes filled with intracellular solution varied between 2 and 4 M Ω . Synaptic currents were monitored with a Multiclamp 700B amplifier (Molecular Devices). The frequency, duration, and magnitude of the extracellular stimulation were controlled with a Model 2100 Isolated Pulse Stimulator (A-M Systems, Inc.) synchronized with Clampex 10 data acquisition software (Molecular Devices). For voltage-clamp recordings of excitatory transmission, a whole-cell pipette solution was used containing (in mM) 135 Cs-Methanesulfonate, 8 CsCl, 10 Hepes, 0.25 EGTA, 0.3 Na₂GTP, 2 MgATP, 7 phosphocreatine, and 10 QX-314 (Thermo Fisher Scientific; Cat# 1014; pH 7.3, adjusted with CsOH and 303 Osm). For voltage-clamp recordings of inhibitory transmission, a whole-cell pipette solution was used containing (in mM) 146 CsCl, 10 Hepes, 0.25 EGTA, 2 MgATP, 0.3 Na₂GTP, 7 phosphocreatine, and 10 QX-314 (pH 7.3, adjusted with CsOH and 303 Osm). The external bath solution contained (in mM) 140 NaCl, 5 KCl, 2 CaCl₂, 0.8 MgCl₂, 10 Hepes, and 10 glucose (pH 7.4, adjusted with NaOH). AMPAR- and NMDAR-EPSC postsynaptic currents were pharmacologically isolated by adding the γ -aminobutyric acid A receptor blocker picrotoxin (50 μ M; Tocris; Cat# 1128) to the extracellular bath solution. AMPAR-EPSCs and mEPSC recordings were performed while holding the cell at -70 mV and NMDAR-EPSCs at +40 mV. γ -aminobutyric acid receptor IPSCs were isolated by adding AP5 (50 μ M; Tocris Cat# 0106) and CNQX (10 μ M; Tocris; Cat# 1045) to the extracellular solution. Spontaneous miniature postsynaptic currents (mEPSCs) were monitored in the presence of tetrodotoxin (1 μ M; Tocris; Cat# 1069) to block action potentials, at -70-mV holding potential. Synaptic currents were sampled at 10 kHz and analyzed offline using Clampfit 10 software (Molecular Devices). Miniature events were analyzed using the template matching search and a minimal threshold of 5 pA, and each event was visually inspected for inclusion or rejection by an experimenter blind to the recording condition.

Slice electrophysiology

For acute slice electrophysiology, lentiviruses were injected into P0 mice as described below, and infected CA1 pyramidal neurons were analyzed at P21-25. Transverse hippocampal slices (300 μ m) were rapidly prepared by cutting in ice-cold solution containing (in mM) 228 Sucrose, 2.5 KCl, 1 NaH₂PO₄, 26 NaHCO₃, 0.5 CaCl₂, 7 MgSO₄, and 11 D-Glucose saturated with 95% O₂/5% CO₂. Slices were transferred to a holding chamber containing artificial cerebrospinal fluid (ACSF; in mM): 119 NaCl, 2.5 KCl, 1 NaH₂PO₄, 26 NaHCO₃, 2.5 CaCl₂, 1.3 MgSO₄, 11 D-Glucose, and ~290 mOsm. Slices were recovered at 32°C for 30 min, followed by holding at room temperature for 1 h. Acute slices were transferred to a recording chamber continuously perfused with oxygenated ACSF (1.5 ml/min) maintained at 32°C. Neurons were clamped at -70 mV, and two-pathways of extracellular-evoked EPSCs in hippocampal slices were monitored. AMPAR-EPSCs were evoked by electrical stimulation using tungsten electrodes (Matrix electrode, 2 \times 1; FHC; Cat# MX21AEW[RT2]) positioned at the stratum (S.) radiatum proximal to CA3, and the S. lacunosum-moleculare proximal to the molecular layer of the

dentate gyrus. NMDAR EPSCs were measured in the same cells by switching holding potentials from -70 mV to +40 mV. Peak amplitude of NMDAR EPSCs was measured 50 ms after the stimulation artifact.

IHC

Mice were anesthetized with isoflurane and perfused with 10 ml ACSF, followed by 30 ml 4% PFA/PBS. The brains were postfixed 1 h at 4°C, transferred to 30% sucrose/PBS for cryoprotection, and sliced at 40 μ m on a cryostat. The free-floating coronal sections were blocked for 1 h in blocking buffer (4% BSA [Sigma; Cat# 10735086001]/3% goat serum [Sigma; Cat# G9023]/0.1% Triton X-100/0.05% sodium azide/PBS) and incubated overnight with primary antibodies diluted in blocking solution, followed by 3 \times 5-min washes in PBS and 2-h incubation with corresponding fluorescently labeled secondary antibodies in blocking buffer, and counterstained with DAPI in PBS for 15 min at room temperature (Sigma; Cat# 10236276001). Samples were washed 5 \times 5 min and mounted on glass slides coated in 0.1% Triton X-100/PBS, dried briefly, and covered with Fluoromount-G (Southern Biotech; Cat# 0100-01) and cover glass (VWR; Cat# 48393241).

Sparse lentiviral infections in vivo

P0 C57BL/6 pups were anesthetized on ice for 5 min and subsequently placed in a homemade clay mold to secure their head in place. Lentivirus was previously loaded and injected with a glass pipette connected to an infusion pump (Harvard Apparatus) completely continuous with mineral oil. A stereotactic injection rig (Kopf) was used to target injections. Lentiviruses were diluted to a 10⁷ IU/ml titer, and 0.3 μ l was injected at the following stereotactic coordinates from the λ at a 1 μ l/min rate: A-P 1.0, M-L 0.9, and D-V three subsequent injections at 1.4, 1.2, and 1.0. Pups then recovered in a clean cage placed on a heating pad and were transferred back to their home cage using cage bedding after completely recovering. Pups were anesthetized individually and returned immediately following recovery to prevent all pups from being removed from the cage at once and excess stress to the female mice.

Monosynaptic retrograde rabies tracing

Complementing AAVs containing CAG-FLEX-TCB-mCherry and CAG-FLEX-RG were generated at the Janelia Farm Viral Core Facility in capsid 2/5 and 2/8, respectively, and injected in P21 mice. Adult mice were stereotactically injected by anesthetizing with an intraperitoneal injection of 2,2,2-tribromoethanol (Avertin; Sigma; Cat# T48402; 250 mg/kg). Mouse heads were shaved, the shaved area was cleaned with Betadine, lubricant was placed on eyes (Puralube Vet Ointment), and heads were secured in a stereotactic injection rig (Kopf), and a small incision was made through the scalp with sterilized tools. Viral solution was injected with a glass pipette at a flow rate of 0.15 μ l/min and 0.5 μ l volume per injection. Coordinates used for unilateral CA1 injections were AP -1.80 mm, ML +/-1.35 mm, DV -1.25 mm. The injection pipette was left at the injection site for 5 min after the injection to prevent the spread of virus into neighboring brain regions. Incisions were sutured and sealed with Vetbond

tissue adhesive (1469SB), and mice were subsequently removed from the stereotactic injection rig. Mice were monitored in a warmed recovery cage until full recovery, based on locomotor activity and awareness. RbV-CVS-N2c-deltaG-GFP (EnvA) was produced at the Janelia Farm Viral core facility and injected 2 wk after AAV injections at an infectious titer of 10^8 IU/ml as described above. Mice were subsequently perfused and analyzed 5 d after rabies injection.

Imaging

Images were acquired using a Nikon A1 Eclipse Ti confocal microscope with a $10\times$ (NA = 0.45), $20\times$ (NA = 0.75), and $60\times$ (NA = 1.4) objective, operated by NIS-Elements AR v4.5 acquisition software. Laser intensities and acquisition settings were established for individual channels and applied to entire experiments. Image analysis was conducted using NeuronStudio (CNIC), NeuroLucida 360 (MBF Biosciences), Nikon Elements, ImageJ, and Adobe Photoshop.

Biocytin labeling, spine imaging, and 3D reconstructions of CA1 pyramidal neurons

Cesium methanesulfonate internal solution was made as described above, with 2 mg/ml Biocytin (Sigma; Cat# B4261). Following whole-cell voltage-clamp recordings, slices were transferred to 4% PFA/PBS and fixed overnight at 4°C. Sections were washed 3×5 min with PBS, permeabilized in 0.3% Triton X-100/PBS at room temperature for 30 min, and blocked in 5% normal goat serum/0.1% Triton X-100/PBS at room temperature for 1 h. Subsequently, slices were incubated in Streptavidin Alexa Fluor 488 or 555 (Invitrogen; Cat# S21381) diluted 1:1,000 in 5% normal goat serum/0.1% Triton X-100/PBS at 4°C overnight, washed 5×5 min with PBS, and mounted with 0-thickness cover-glass (Assistent; Cat# 01105209). For spine imaging and categorization, z-stacks were collected at 0.2- μm intervals at 0.08- $\mu\text{m}/\text{pixel}$ resolution with $2\times$ averaging. For full neuron reconstructions and dendritic arbor tracing, images were collected with a $20\times$ objective, together with image tiling and 3- μm -interval z-stacks to cover the entire neuron in the x, y, and z dimensions. Data analysis and 3D reconstructions were performed with NeuronStudio (CNIC) and NeuroLucida360 software (MBF Bioscience).

STORM imaging

Primary hippocampal cultures from CD1 mice were infected with lentiviruses encoding indicated Hr1-nanobody-HA-YFP fusions at DIV3 and subsequently labeled at DIV14 as described above for HA mouse (Covance; Cat# MMS101R; 1:2,500), HA rabbit (Cell Signaling Technologies; Cat# 3724; 1:2,500), Homer1 rabbit (Synaptic Systems; Cat# 160003; 1:2,500), gephyrin mouse (Synaptic Systems; Cat# 147111; 1:5,000), vGLUT1 guinea pig (Millipore Cat# AB5905; 1:2,500), vGAT guinea pig (Millipore Cat# AB5062P; 1:2,500), and corresponding CF568 (Biotium; 1:5,000) or Alexa Fluor 647 (Thermo Fisher Scientific; 1:5,000) secondary antibodies. STORM data acquisition and analysis were performed using a Vutara352 nanoscope with a fixed $60\times$ objective in the following blinking buffer: 50 mM Tris-HCl (pH 8.0), 10 mM NaCl, 10% (wt/vol) glucose, 1% (vol/

vol) 2-mercaptoethanol, 20 mM cystamine (Sigma; Cat# 30070), 168.8 a.u. Glucose oxidase (Sigma; Cat# G2133), and 1,404 a.u. catalase (Sigma; Cat# C40). Images were acquired with a 30- μm pinhole in an interleaved capture mode with 4,000 frames per probe at a 20-ms exposure time. All images were processed uniformly with 50% denoising and analyzed with Vutara SRX software.

Transmission EM

Cultured neurons were fixed in 2.5% glutaraldehyde in 0.1 M sodium cacodylate buffer, pH 7.4, at room temperature for 1 h. After cells were rinsed in the same buffer twice, they were further postfixated in 1% OsO₄, 0.8% potassium ferricyanide in 0.1 M cacodylate buffer at room temperature for 1 h. Cells were further stained en bloc with 2% aqueous uranyl acetate for 30 min, subsequently dehydrated in a graded series of ethanol to 100%, and embedded in EMbed 812 resin. Blocks were polymerized in 60°C oven overnight. Thin sections (60 nm) were cut by a Leica UC7 ultramicrotome and poststained with 2% uranyl acetate and lead citrate. Sample sections were examined with a FEI Tecnai transmission EM at accelerating voltage of 80 kV. Digital images were recorded with an Olympus Morada CCD camera and iTEM imaging software. Images were analyzed with ImageJ, and docked presynaptic vesicles were considered 5 nm or closer to the presynaptic active zone membrane.

Statistics

Experiments were performed in a blinded manner whenever possible by coding viral solutions. All data are expressed as means \pm SEM and represent the results of at least three independent biological replicates. Statistical significance was determined using the two-tailed Student's *t* test, one-way ANOVA, or two-way ANOVA with post hoc Tukey tests for multiple comparisons, as indicated in the figure legends. Data analysis and statistics were performed with Microsoft Excel and GraphPad Prism 8.0.

Online supplemental material

Fig. S1 describes additional characterization of PDE fusion construct enzymatic function, expression, and subcellular localization. Fig. S2 contains additional in vitro neuronal morphology, synapse morphology via EM, and intrinsic electrical properties and relates to main Fig. 1 and Fig. 2. Fig. S3 depicts Homer1 nanobody fusion localization to dendritic spine heads via confocal microscopy, additional STORM localization data, and low-power EM images and relates to main Fig. 2 and Fig. 4. Fig. S4 describes additional morphological parameters of patched CA1 pyramidal neurons and relates to main Fig. 5, Fig. 6, and Fig. 7. Fig. S5 contains mEPSC amplitude measurements, intrinsic electrical properties of CA1 pyramidal neurons in acute slices, and a schematic diagram and additional images from rabies virus retrograde tracing experiments and relates to main Fig. 6, Fig. 7, and Fig. 8.

Acknowledgments

We thank Irina Huryeva and Shaleeka Cornelius for experimental support.

This study was supported by grants from the National Institutes of Health (K99-MH117235 to R. Sando).

The authors declare no competing financial interests.

Author contributions: R. Sando and T.C. Südhof designed the experiments and analyzed the results; R. Sando, M.L. Ho, and X. Liu performed the experiments, and R. Sando and T.C. Südhof wrote the manuscript with input from all authors.

Submitted: 23 September 2021

Revised: 15 November 2021

Accepted: 30 November 2021

References

- Anderson, G.R., S. Maxeiner, R. Sando, T. Tsetsenis, R.C. Malenka, and T.C. Südhof. 2017. Postsynaptic adhesion GPCR latrophilin-2 mediates target recognition in entorhinal-hippocampal synapse assembly. *J. Cell Biol.* 216:3831–3846. <https://doi.org/10.1083/jcb.201703042>
- Araç, D., and J. Li. 2019. Teneurins and latrophilins: two giants meet at the synapse. *Curr. Opin. Struct. Biol.* 54:141–151. <https://doi.org/10.1016/j.sbi.2019.01.028>
- Argyrousi, E.K., P.R.A. Heckman, and J. Prickaerts. 2020. Role of cyclic nucleotides and their downstream signaling cascades in memory function: Being at the right time at the right spot. *Neurosci. Biobehav. Rev.* 113: 12–38. <https://doi.org/10.1016/j.neubiorev.2020.02.004>
- Attardo, A., J.E. Fitzgerald, and M.J. Schnitzer. 2015. Impermanence of dendritic spines in live adult CA1 hippocampus. *Nature.* 523:592–596. <https://doi.org/10.1038/nature14467>
- Averaimo, S., and X. Nicol. 2014. Intermingled cAMP, cGMP and calcium spatiotemporal dynamics in developing neuronal circuits. *Front. Cell. Neurosci.* 8:376. <https://doi.org/10.3389/fncel.2014.00376>
- Biederer, T., P.S. Kaeser, and T.A. Blanpied. 2017. Transcellular Nanoalignment of Synaptic Function. *Neuron.* 96:680–696. <https://doi.org/10.1016/j.neuron.2017.10.006>
- Boczek, T., E.G. Cameron, W. Yu, X. Xia, S.H. Shah, B. Castillo Chabeco, J. Galvao, M. Nahmou, J. Li, H. Thakur, et al. 2019. Regulation of Neuronal Survival and Axon Growth by a Perinuclear cAMP Compartment. *J. Neurosci.* 39: 5466–5480. <https://doi.org/10.1523/JNEUROSCI.2752-18.2019>
- Bolshakov, V.Y., H. Golan, E.R. Kandel, and S.A. Siegelbaum. 1997. Recruitment of new sites of synaptic transmission during the cAMP-dependent late phase of LTP at CA3-CA1 synapses in the hippocampus. *Neuron.* 19: 635–651. [https://doi.org/10.1016/S0896-6273\(00\)80377-3](https://doi.org/10.1016/S0896-6273(00)80377-3)
- Bourgeois, J.P., and P. Rakic. 1993. Changes of synaptic density in the primary visual cortex of the macaque monkey from fetal to adult stage. *J. Neurosci.* 13:2801–2820. <https://doi.org/10.1523/JNEUROSCI.13-07-02801.1993>
- Callaway, E.M. 2008. Transneuronal circuit tracing with neurotropic viruses. *Curr. Opin. Neurobiol.* 18:617–623. <https://doi.org/10.1016/j.conb.2009.03.007>
- Chanda, S., W.D. Hale, B. Zhang, M. Wernig, and T.C. Südhof. 2017. Unique versus Redundant Functions of Neuroigin Genes in Shaping Excitatory and Inhibitory Synapse Properties. *J. Neurosci.* 37:6816–6836. <https://doi.org/10.1523/JNEUROSCI.0125-17.2017>
- Chetkovich, D.M., R. Gray, D. Johnston, and J.D. Sweatt. 1991. N-methyl-D-aspartate receptor activation increases cAMP levels and voltage-gated Ca²⁺ channel activity in area CA1 of hippocampus. *Proc. Natl. Acad. Sci. USA.* 88:6467–6471. <https://doi.org/10.1073/pnas.88.15.6467>
- Chevalleyre, V., B.D. Heifets, P.S. Kaeser, T.C. Südhof, and P.E. Castillo. 2007. Endocannabinoid-mediated long-term plasticity requires cAMP/PKA signaling and RIM1 α . *Neuron.* 54:801–812. <https://doi.org/10.1016/j.neuron.2007.05.020>
- Collins, C.A., Y.P. Wairkar, S.L. Johnson, and A. DiAntonio. 2006. Highwire restrains synaptic growth by attenuating a MAP kinase signal. *Neuron.* 51:57–69. <https://doi.org/10.1016/j.neuron.2006.05.026>
- Connor, S.A., J. Elegeert, Y. Xie, and A.M. Craig. 2019. Pumping the brakes: suppression of synapse development by MDGA-neuroigin interactions. *Curr. Opin. Neurobiol.* 57:71–80. <https://doi.org/10.1016/j.conb.2019.01.002>
- Dalton, G.D., and W.L. Dewey. 2006. Protein kinase inhibitor peptide (PKI): a family of endogenous neuropeptides that modulate neuronal cAMP-dependent protein kinase function. *Neuropeptides.* 40:23–34. <https://doi.org/10.1016/j.npep.2005.10.002>
- de Wit, J., and A. Ghosh. 2016. Specification of synaptic connectivity by cell surface interactions. *Nat. Rev. Neurosci.* 17:22–35. <https://doi.org/10.1038/nrn.2015.3>
- Deisseroth, K., H. Bitto, and R.W. Tsien. 1996. Signaling from synapse to nucleus: postsynaptic CREB phosphorylation during multiple forms of hippocampal synaptic plasticity. *Neuron.* 16:89–101. [https://doi.org/10.1016/S0896-6273\(00\)80026-4](https://doi.org/10.1016/S0896-6273(00)80026-4)
- Dong, J.X., Y. Lee, M. Kirmiz, S. Palacio, C. Dumitras, C.M. Moreno, R. Sando, L.F. Santana, T.C. Südhof, B. Gong, et al. 2019. A toolbox of nanobodies developed and validated for use as intrabodies and nanoscale immunolabels in mammalian brain neurons. *eLife.* 8:e48750. <https://doi.org/10.7554/eLife.48750>
- Duffy, S.N., and P.V. Nguyen. 2003. Postsynaptic application of a peptide inhibitor of cAMP-dependent protein kinase blocks expression of long-lasting synaptic potentiation in hippocampal neurons. *J. Neurosci.* 23: 1142–1150. <https://doi.org/10.1523/JNEUROSCI.23-04-01142.2003>
- Frey, U., Y.Y. Huang, and E.R. Kandel. 1993. Effects of cAMP simulate a late stage of LTP in hippocampal CA1 neurons. *Science.* 260:1661–1664. <https://doi.org/10.1126/science.8389057>
- Gorshkov, K., S. Mehta, S. Ramamurthy, G.V. Ronnett, F.Q. Zhou, and J. Zhang. 2017. AKAP-mediated feedback control of cAMP gradients in developing hippocampal neurons. *Nat. Chem. Biol.* 13:425–431. <https://doi.org/10.1038/nchembio.2298>
- Hashimoto, Y., K. Nasrallah, K.R. Jensen, A.E. Chávez, D. Carrera, and P.E. Castillo. 2017. LTP at Hilar Mossy Cell-Dentate Granule Cell Synapses Modulates Dentate Gyrus Output by Increasing Excitation/Inhibition Balance. *Neuron.* 95:928–943.e3. <https://doi.org/10.1016/j.neuron.2017.07.028>
- Hetman, J.M., S.H. Soderling, N.A. Glavas, and J.A. Beavo. 2000. Cloning and characterization of PDE7B, a cAMP-specific phosphodiesterase. *Proc. Natl. Acad. Sci. USA.* 97:472–476. <https://doi.org/10.1073/pnas.97.1.472>
- Höpker, V.H., D. Shewan, M. Tessier-Lavigne, M. Poo, and C. Holt. 1999. Growth-cone attraction to netrin-1 is converted to repulsion by laminin-1. *Nature.* 401:69–73. <https://doi.org/10.1038/43441>
- Hopkins, W.F., and D. Johnston. 1988. Noradrenergic enhancement of long-term potentiation at mossy fiber synapses in the hippocampus. *J. Neurophysiol.* 59:667–687. <https://doi.org/10.1152/jn.1988.59.2.667>
- Huttenlocher, P.R., C. de Courten, L.J. Garey, and H. Van der Loos. 1982. Synaptogenesis in human visual cortex—evidence for synapse elimination during normal development. *Neurosci. Lett.* 33:247–252. [https://doi.org/10.1016/0304-3940\(82\)90379-2](https://doi.org/10.1016/0304-3940(82)90379-2)
- Imai, T., M. Suzuki, and H. Sakano. 2006. Odorant receptor-derived cAMP signals direct axonal targeting. *Science.* 314:657–661. <https://doi.org/10.1126/science.1131794>
- Jang, S., H. Lee, and E. Kim. 2017. Synaptic adhesion molecules and excitatory synaptic transmission. *Curr. Opin. Neurobiol.* 45:45–50. <https://doi.org/10.1016/j.conb.2017.03.005>
- Jiang, X., R. Sando, and T.C. Südhof. 2021. Multiple signaling pathways are essential for synapse formation induced by synaptic adhesion molecules. *Proc. Natl. Acad. Sci. USA.* 118:e2000173118. <https://doi.org/10.1073/pnas.2000173118>
- Johnstone, T.B., S.R. Agarwal, R.D. Harvey, and R.S. Ostrom. 2018. cAMP Signaling Compartmentation: Adenylyl Cyclases as Anchors of Dynamic Signaling Complexes. *Mol. Pharmacol.* 93:270–276. <https://doi.org/10.1124/mol.117.110825>
- Kasem, E., T. Kurihara, and K. Tabuchi. 2018. Neurexins and neuropsychiatric disorders. *Neurosci. Res.* 127:53–60. <https://doi.org/10.1016/j.neures.2017.10.012>
- Kennedy, M.B. 2000. Signal-processing machines at the postsynaptic density. *Science.* 290:750–754. <https://doi.org/10.1126/science.290.5492.750>
- Kwon, H.B., and B.L. Sabatini. 2011. Glutamate induces de novo growth of functional spines in developing cortex. *Nature.* 474:100–104. <https://doi.org/10.1038/nature09986>
- Lie, E., Y. Li, R. Kim, and E. Kim. 2018. SALM/Lrfrn Family Synaptic Adhesion Molecules. *Front. Mol. Neurosci.* 11:105. <https://doi.org/10.3389/fnmol.2018.00105>
- Mai, J., L. Fok, H. Gao, X. Zhang, and M.M. Poo. 2009. Axon initiation and growth cone turning on bound protein gradients. *J. Neurosci.* 29: 7450–7458. <https://doi.org/10.1523/JNEUROSCI.1121-09.2009>
- Nair, R., J. Lauks, S. Jung, N.E. Cooke, H. de Wit, N. Brose, M.W. Kilimann, M. Verhage, and J. Rhee. 2013. Neurobeachin regulates neurotransmitter receptor trafficking to synapses. *J. Cell Biol.* 200:61–80. <https://doi.org/10.1083/jcb.201207113>
- Nusser, Z. 2018. Creating diverse synapses from the same molecules. *Curr. Opin. Neurobiol.* 51:8–15. <https://doi.org/10.1016/j.conb.2018.01.001>

- Patriarchi, T., O.R. Buonarati, and J.W. Hell. 2018. Postsynaptic localization and regulation of AMPA receptors and Cav1.2 by β 2 adrenergic receptor/PKA and Ca^{2+} /CaMKII signaling. *EMBO J.* 37:e99771. <https://doi.org/10.15252/embj.201899771>
- Petanjek, Z., M. Judaš, G. Šimic, M.R. Rasin, H.B. Uylings, P. Rakic, and I. Kostovic. 2011. Extraordinary neoteny of synaptic spines in the human prefrontal cortex. *Proc. Natl. Acad. Sci. USA.* 108:13281–13286. <https://doi.org/10.1073/pnas.1105108108>
- Pfeiffer, T., S. Poll, S. Bancelin, J. Angibaud, V.K. Inavalli, K. Keppler, M. Mittag, M. Fuhrmann, and U.V. Nägerl. 2018. Chronic 2P-STED imaging reveals high turnover of dendritic spines in the hippocampus in vivo. *eLife.* 7:e34700. <https://doi.org/10.7554/eLife.34700>
- Qiao, Q., L. Ma, W. Li, J.W. Tsai, G. Yang, and W.B. Gan. 2016. Long-term stability of axonal boutons in the mouse barrel cortex. *Dev. Neurobiol.* 76:252–261. <https://doi.org/10.1002/dneu.22311>
- Ribic, A., and T. Biederer. 2019. Emerging Roles of Synapse Organizers in the Regulation of Critical Periods. *Neural Plast.* 2019:1538137. <https://doi.org/10.1155/2019/1538137>
- Russo, A., P. Goel, E.J. Brace, C. Buser, D. Dickman, and A. DiAntonio. 2019. The E3 ligase Highwire promotes synaptic transmission by targeting the NAD-synthesizing enzyme dNmnat. *EMBO Rep.* 20:e46975. <https://doi.org/10.15252/embr.201846975>
- Sanderson, J.L., J.D. Scott, and M.L. Dell'Acqua. 2018. Control of Homeostatic Synaptic Plasticity by AKAP-Anchored Kinase and Phosphatase Regulation of Ca^{2+} -Permeable AMPA Receptors. *J. Neurosci.* 38:2863–2876. <https://doi.org/10.1523/JNEUROSCI.2362-17.2018>
- Sando, R., X. Jiang, and T.C. Südhof. 2019. Latrophilin GPCRs direct synapse specificity by coincident binding of FLRTs and teneurins. *Science.* 363:eav7969. <https://doi.org/10.1126/science.aav7969>
- Sando, R., and T.C. Südhof. 2021. Latrophilin GPCR signaling mediates synapse formation. *eLife.* 10:e65717. <https://doi.org/10.7554/eLife.65717>
- Sanes, J.R., and M. Yamagata. 2009. Many paths to synaptic specificity. *Annu. Rev. Cell Dev. Biol.* 25:161–195. <https://doi.org/10.1146/annurev.cellbio.24.110707.175402>
- Shelly, M., B.K. Lim, L. Cancedda, S.C. Heilshorn, H. Gao, and M.M. Poo. 2010. Local and long-range reciprocal regulation of cAMP and cGMP in axon/dendrite formation. *Science.* 327:547–552. <https://doi.org/10.1126/science.1179735>
- Song, H.J., G.L. Ming, and M.M. Poo. 1997. cAMP-induced switching in turning direction of nerve growth cones. *Nature.* 388:275–279. <https://doi.org/10.1038/40864>
- Südhof, T.C. 2017. Synaptic Neurexin Complexes: A Molecular Code for the Logic of Neural Circuits. *Cell.* 171:745–769. <https://doi.org/10.1016/j.cell.2017.10.024>
- Südhof, T.C. 2018. Towards an understanding of synapse formation. *Neuron.* 100:276–293. <https://doi.org/10.1016/j.neuron.2018.09.040>
- Südhof, T.C. 2021. The cell biology of synapse formation. *J. Cell Biol.* 220:e202103052. <https://doi.org/10.1083/jcb.202103052>
- Suzuki, K., J. Elegeert, I. Song, H. Sasakura, O. Senkov, K. Matsuda, W. Kakegawa, A.J. Clayton, V.T. Chang, M. Ferrer-Ferrer, et al. 2020. A synthetic synaptic organizer protein restores glutamatergic neuronal circuits. *Science.* 369:eabb4853. <https://doi.org/10.1126/science.abb4853>
- Wan, H.I., A. DiAntonio, R.D. Fetter, K. Bergstrom, R. Strauss, and C.S. Goodman. 2000. Highwire regulates synaptic growth in Drosophila. *Neuron.* 26:313–329. [https://doi.org/10.1016/S0896-6273\(00\)81166-6](https://doi.org/10.1016/S0896-6273(00)81166-6)
- Weisskopf, M.G., P.E. Castillo, R.A. Zalutsky, and R.A. Nicoll. 1994. Mediation of hippocampal mossy fiber long-term potentiation by cyclic AMP. *Science.* 265:1878–1882. <https://doi.org/10.1126/science.7916482>
- West, A.E., W.G. Chen, M.B. Dalva, R.E. Dolmetsch, J.M. Kornhauser, A.J. Shaywitz, M.A. Takasu, X. Tao, and M.E. Greenberg. 2001. Calcium regulation of neuronal gene expression. *Proc. Natl. Acad. Sci. USA.* 98:11024–11031. <https://doi.org/10.1073/pnas.191352298>
- Wiegert, J.S., M. Pulin, C.E. Gee, and T.G. Oertner. 2018. The fate of hippocampal synapses depends on the sequence of plasticity-inducing events. *eLife.* 7:e39151. <https://doi.org/10.7554/eLife.39151>
- Worley, P.F., W. Zeng, G. Huang, J.Y. Kim, D.M. Shin, M.S. Kim, J.P. Yuan, K. Kiselyov, and S. Muallem. 2007. Homer proteins in Ca^{2+} signaling by excitable and non-excitable cells. *Cell Calcium.* 42:363–371. <https://doi.org/10.1016/j.ceca.2007.05.007>
- Xiao, B., J.C. Tu, and P.F. Worley. 2000. Homer: a link between neural activity and glutamate receptor function. *Curr. Opin. Neurobiol.* 10:370–374. [https://doi.org/10.1016/S0959-4388\(00\)00087-8](https://doi.org/10.1016/S0959-4388(00)00087-8)
- Yeckel, M.F., A. Kapur, and D. Johnston. 1999. Multiple forms of LTP in hippocampal CA3 neurons use a common postsynaptic mechanism. *Nat. Neurosci.* 2:625–633. <https://doi.org/10.1038/10180>
- Yuzaki, M. 2018. Two Classes of Secreted Synaptic Organizers in the Central Nervous System. *Annu. Rev. Physiol.* 80:243–262. <https://doi.org/10.1146/annurev-physiol-021317-121322>
- Zaccolo, M., A. Zerio, and M.J. Lobo. 2021. Subcellular Organization of the cAMP Signaling Pathway. *Pharmacol. Rev.* 73:278–309. <https://doi.org/10.1124/pharmrev.120.000086>

Supplemental material

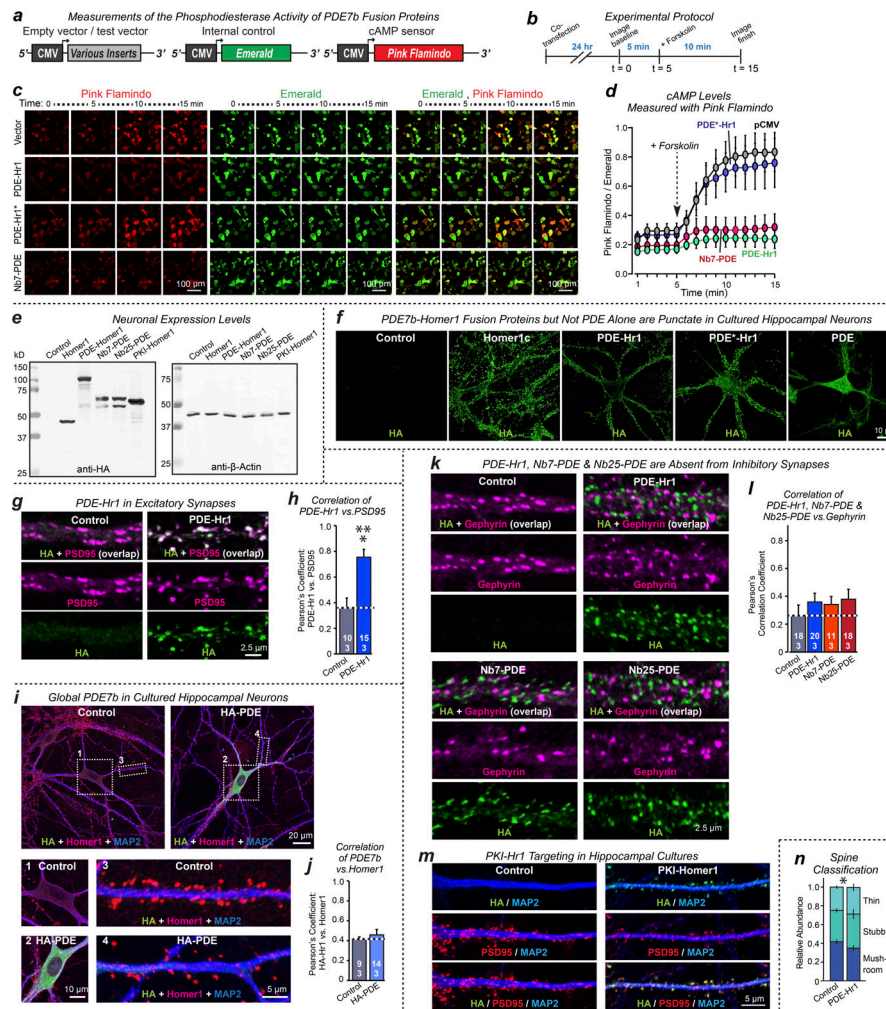


Figure S1. Detailed analyses documenting enzymatic activity of PDE-Hr1 but not PDE*-Hr1 and the expression and synaptic localization of various SynTAMs that are targeted to developing postsynaptic specializations of excitatory synapses but excluded from inhibitory synapses, as well as effects of the PDE-Hr1 SynTAM on spine types. (a) Diagram of constructs used to test the cAMP hydrolysis activity of SynTAMs. The fluorescent cAMP sensor Pink Flamindo was coexpressed with Emerald GFP as an internal control and with the PDE-Hr1, PDE*-Hr1, and Nb7-PDE SynTAMs in HEK293T cells. Empty pCMV vector was used as a control. (b) Experimental strategy. HEK293T cells were cotransfected with Pink Flamindo, Emerald GFP, and the indicated PDE fusion proteins or empty vector (Control). Live imaging was conducted 24 h after transfection. Baseline Pink Flamindo/Emerald GFP intensity was measured for 5 min, and cells were stimulated with 100 μ M forskolin (FSK) and imaged for an additional 10 min. (c) Representative Pink Flamindo (left), Emerald GFP (middle), and merged fluorescence images (right). (d) Quantification of the ratio of Pink Flamindo/Emerald GFP signal over time. Note that coexpression of PDE-Hr1 or Nb7-PDE abolishes the FSK-induced increase in Pink Flamindo signal, whereas PDE*-Hr1 is inactive and does not differ from the empty pCMV vector. (e) IB analysis of the indicated HA-tagged SynTAMs and HA-Homer1. Proteins were expressed via lentiviruses in primary hippocampal cultures (β -actin, loading control). (f) Synaptic targeting of Homer1c, PDE-Hr1, and PDE*-Hr1 SynTAMs in cultured hippocampal neurons. Images show the HA-only signal for panels in Fig. 1 b, which depicts the merged images. Cultured hippocampal neurons were infected with lentiviruses encoding the indicated proteins and were immunolabeled for HA and MAP2 together with DAPI. Note that Homer1c and SynTAM proteins are equally targeted to postsynaptic specializations, whereas PDE alone fills the somatic cytosol. Control conditions were cultures infected with empty lentiviral particles that were packaged in parallel with test lentiviruses. (g and h) PDE-Hr1 SynTAM localizes with the endogenous excitatory postsynaptic protein PSD-95. (g) Representative high-magnification images. (h) Summary graph of Pearson's correlation coefficient demonstrating nearly perfect colocalization of PDE-Hr1 with endogenous PSD-95. (i and j) HA-tagged PDE7b expressed alone is predominately localized to the soma and primary dendrites of neurons and does not significantly diffuse into distal dendrites and postsynaptic spines. Primary hippocampal cultures were infected with lentiviruses encoding HA-PDE7b at DIV3 and colabeled for HA, MAP2, and Homer1c at DIV14. The Pearson's correlation coefficient of HA-PDE7b relative to Homer1c that specifically marks postsynaptic specializations is indistinguishable from Control conditions, which measure background HA signal relative to Homer1c. (i) Representative images; center: high-magnification somatic and dendritic regions corresponding to numbered boxed areas. (j) Summary graph of the correlation coefficient. (k and l) PDE-Hr1, Nb7-PDE, and Nb25-PDE SynTAMs do not colocalize with the inhibitory postsynaptic marker gephyrin. (k) Representative high-magnification images. (l) Summary graph of Pearson's correlation coefficient between the localizations of PDE-Hr1 or the nanobodies and endogenous gephyrin. Control conditions measure background HA staining relative to gephyrin. (m) A PKI-Homer1 fusion protein (PKI-Hr1) colocalizes with the excitatory postsynaptic marker PSD-95 in cultured hippocampal neurons that were infected with lentivirus encoding HA-tagged PKI-Hr1 at DIV3 and coimmunolabeled for HA, MAP2, and PSD-95 at DIV14–16. (n) Quantifications of the relative abundance of mushroom, thin, and stubby dendritic spines from spine quantifications in Fig. 1, c and d. Numerical data are means \pm SEM (numbers of images or cells/independent experiments are shown in bars; for n, n = 3 independent experiments). Statistical significance was assessed by two-tailed Student's *t* test or one-way ANOVA with post hoc Tukey tests for multiple comparisons (***, *P* < 0.001; *, *P* < 0.05). pCMV, plasmid cytomegalovirus.

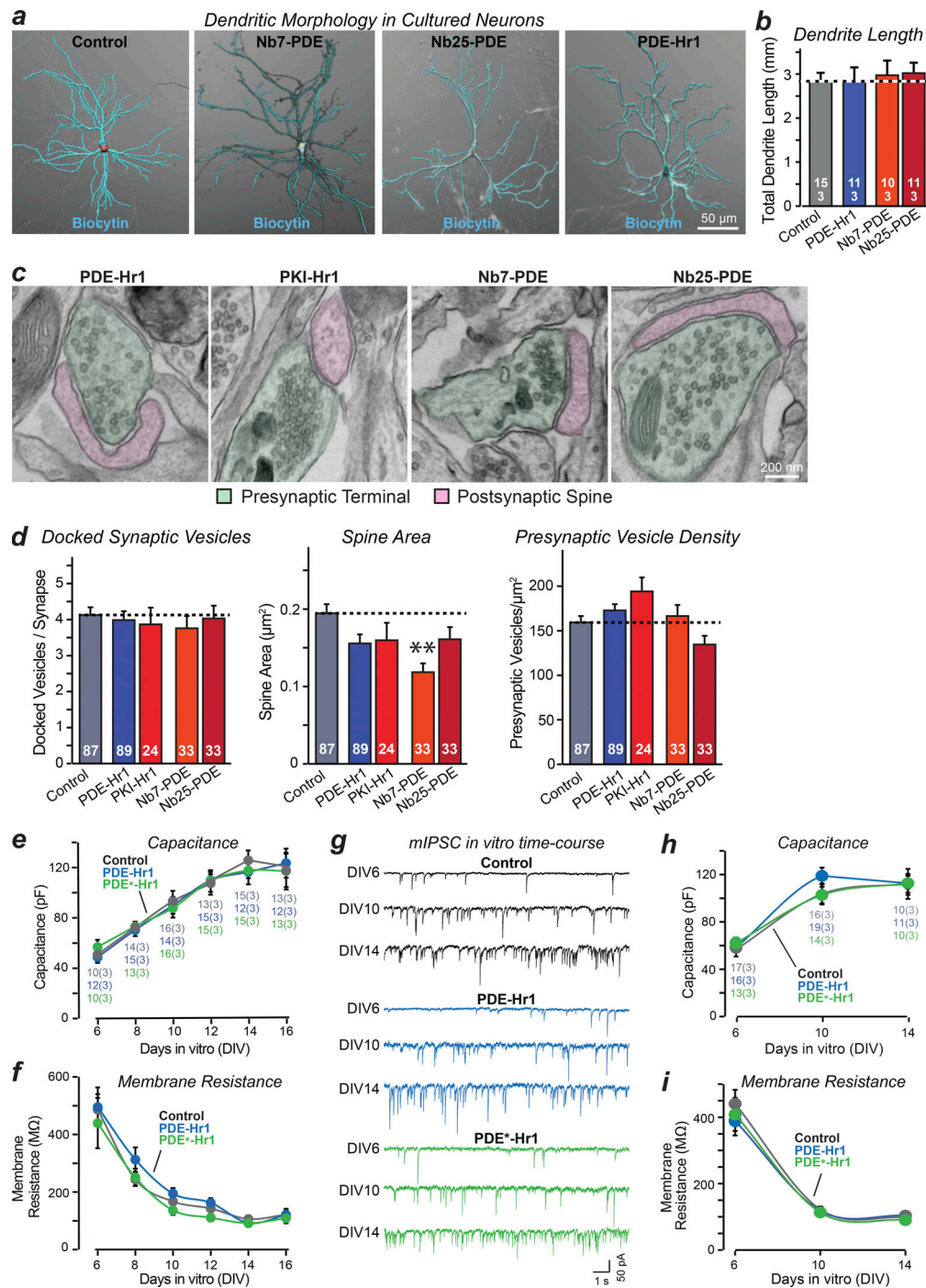


Figure S2. **SynTAMs do not alter dendritic arborization of neurons, additional EM quantifications of synapse parameters, and intrinsic electrical properties and representative mIPSC traces from developmental time course recordings.** (a and b) PDE-Hr1, Nb7-PDE, and Nb25-PDE SynTAMs do not alter the dendritic morphology of hippocampal neurons. Neurons were filled with biocytin during whole-cell voltage-clamp recordings, and dendritic arbors were reconstructed and measured using NeuronStudio. (a) Representative reconstructions. (b) Quantifications of total dendritic length. Control conditions were cultures infected with empty lentiviral particles that were packaged in parallel with experimental lentiviruses. (c and d) Further EM data on the effect of SynTAMs on synapse structure. (c) Additional representative EM images of individual synapses. (d) Summary graphs of the number of docked vesicles, spine area, and presynaptic vesicle density. Data are from the same experiments as shown in Fig. 1, i and j and Fig. 4, d and e. (e and f) Summary graphs of the capacitance (e) and membrane resistance (f) of cultured hippocampal control neurons and neurons expressing PDE-Hr1 or PDE*-Hr1 (from the mEPSC measurements shown in Fig. 2, j-l). Note that SynTAMs have no effect on the dramatic increase in capacitance and decrease in membrane resistance as a function of culture time. These changes reflect the maturation of the neurons during culture. (g) Representative mIPSC traces monitored at DIV6, DIV10, and DIV14 in cultured hippocampal neurons. Data complement the mIPSC frequency and amplitude analyses shown in Fig. 2, m and n. (h and i) Same as a and b, but for the mIPSC analysis as a function of culture time in Fig. 2, m and n. Numerical data in b and d are means \pm SEM (numbers of cells/independent experiments [b] or synapses [d] are shown in bars; numbers in e also apply to f, and numbers in h also apply to i). Statistical significance was assessed by one-way or two-way ANOVA with post hoc Tukey tests for multiple comparisons (**, $P < 0.01$).

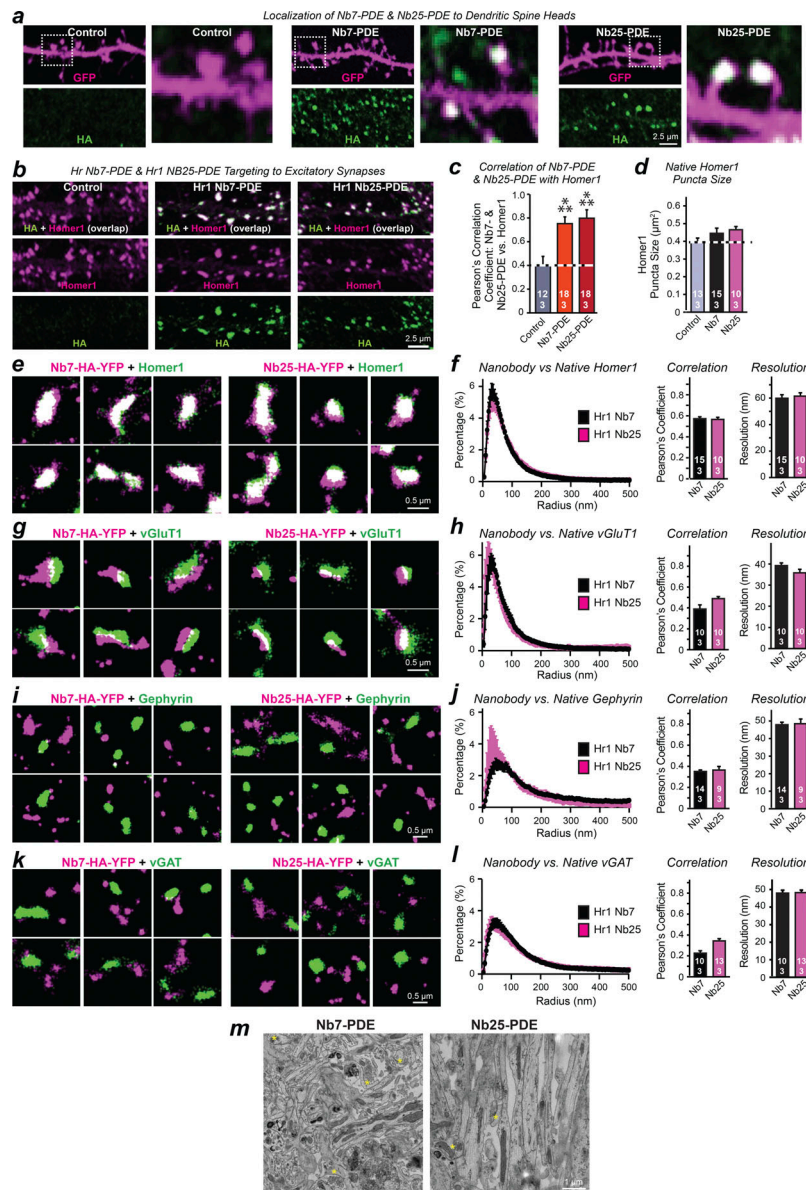


Figure S3. **Nanobody-based, Homer1-targeted SynTAMs (Nb7-PDE and Nb25-PDE) are specifically concentrated in postsynaptic densities of spine heads, STORM super-resolution microscopy demonstrates that Homer-targeted nanobodies do not alter the size of Homer1-positive postsynaptic densities but are localized to excitatory and not inhibitory postsynaptic specializations, and additional EM images are shown.** (a) SynTAMs based on Homer1-targeted nanobodies (Nb7-PDE and Nb25-PDE) are highly concentrated in dendritic spine heads. Primary hippocampal cultures infected with lentiviruses encoding HA-tagged Nb7-PDE or Nb25-PDE were sparsely transfected with GFP to fill the cytosol (single images to the right of each set show an expansion of the boxed area on the left; for merged images, see Fig. 4 a). (b and c) Nb7-PDE and Nb25-PDE SynTAMs precisely colocalize with endogenous Homer1. (b) Representative high-magnification images. (c) Summary graph of Pearson's correlation coefficient between the localizations of the nanobodies and endogenous Homer1. (d) Summary graph of the mean size of Homer1-positive synaptic puncta in control synapses or synapses containing HA-tagged Nb7 and Nb25 nanobodies visualized by STORM super-resolution microscopy. Expression of these nanobodies as HA-YFP fusions does not alter the size of postsynaptic densities. Proteins were expressed via lentiviruses in cultured hippocampal neurons at DIV3 and labeled by ICC for endogenous Homer1 and for exogenous HA-tagged Nb7 or Nb25 at DIV14. For images and cumulative probability plots, see Fig. 4, b and c. (e and f) Super-resolution two-color STORM analyses showing that the localization of Homer1-targeted nanobodies used for SynTAMs (Nb7 and Nb25, both fused to an HA-epitope and to YFP) tightly correlates with that of endogenous Homer1, a marker for excitatory postsynaptic densities. (e) Representative images of HA- and Homer1-positive clusters (magenta, HA-tagged nanobodies; green Homer1; white, overlap). (f) Nearest-neighbor analysis of HA and Homer1 (left), HA-Homer1 Pearson's correlation coefficient (center), and STORM acquisition resolution (right). Nearest-neighbor analysis measures the percentage of HA clusters at a defined distance from Homer1 clusters. (g and h) Same as e and f, except that the analysis was performed for spatial relationship of Homer1-targeted nanobodies with the excitatory presynaptic marker vGluT1. (i and j) Same as e and f, except that the analysis was performed for spatial relationship of Homer1-targeted nanobodies with the inhibitory postsynaptic marker gephyrin. (k and l) Same as e and f, except that the analysis was performed for spatial relationship of Homer1-targeted nanobodies with the inhibitory presynaptic marker vGAT. (m) Low-magnification EM images of cultured hippocampal neurons expressing Nb7-PDE and Nb25-PDE SynTAMs. Quantifications of the synapse density are shown in Fig. 4 e. Yellow asterisks denote synaptic junctions. Data are means \pm SEM (numbers of cells/experiments are indicated in bars). Statistical significance was assessed by two-tailed Student's *t* test or one-way ANOVA with post hoc Tukey tests. (***, $P < 0.001$).

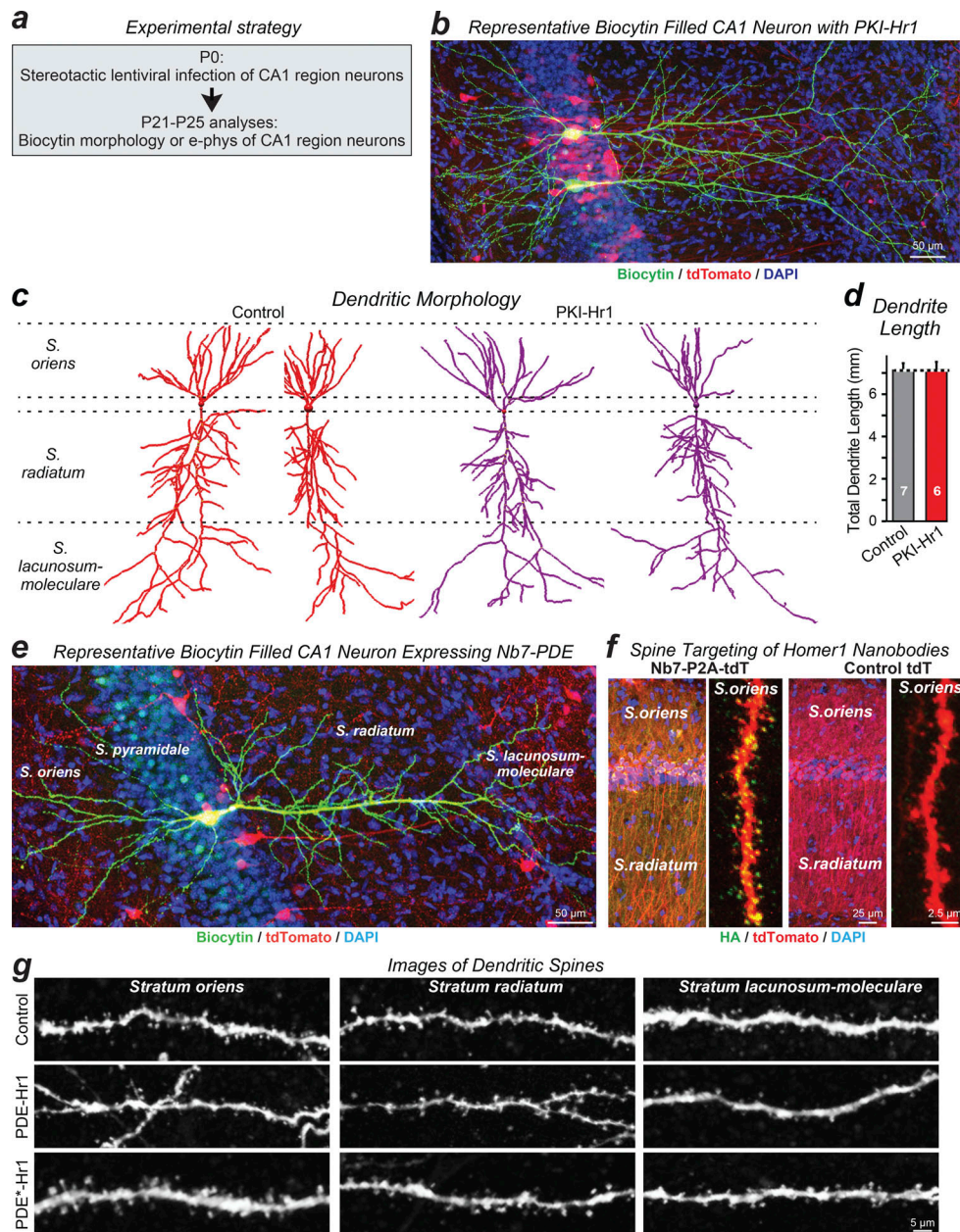


Figure S4. Additional analyses of the effects of SynTAMs expressed in vivo on the morphology of CA1 pyramidal neurons. (a) Experimental strategy for in vivo experiments. CA1 neurons of newborn P0 C57BL/6 mice were sparsely infected with lentiviruses unilaterally, and morphological and electrophysiological (e-phys) analyses were performed at P21–P25. (b) Representative image of two adjacent biocytin-filled CA1 neurons that were infected with a lentivirus encoding PKI-Hr1 and tdTomato. Under the conditions used, CA1 neurons were infected sparsely, and neurons were filled with biocytin during patch-clamp recordings. Note that multiple neurons are infected, as indicated by the red tdTomato fluorescence, but only two neurons were patched. (c and d) Expression of the PKI-Homer1 fusion protein (PKI-Hr1) in pyramidal CA1 neurons of newborn mice does not alter CA1 pyramidal neuron dendritic morphology. (c) Representative 3D reconstructions from biocytin-filled neurons. (d) Quantifications of the combined total dendrite length in the S. oriens, S. radiatum, and S. lacunosum-moleculare (means \pm SEM; statistical significance was assessed by two-tailed Student's *t* test). Control conditions were uninfected cells from slices in the neighboring uninfected hemisphere. (e) Representative image of a biocytin-filled CA1 neuron that was infected with a lentivirus encoding Nb7-PDE (a Homer1-reactive nanobody fused to PDE7b) and tdTomato via a P2A sequence. Under the conditions used, CA1 neurons were infected sparsely, and neurons were filled with biocytin during patch-clamp recordings. (f) A Homer1-reactive nanobody (Hr1 Nb7), when expressed in vivo in CA1 pyramidal neurons with a lentivirus that also expresses tdTomato (tdT), is specifically localized to dendritic spines as illustrated in representative confocal images of neurons expressing tdTomato with (left) or without (right) coexpression of the Homer1 nanobody. C57BL/6 mice were infected at P21 with lentiviruses coexpressing HA-tagged Nb7 and tdTomato via a P2A sequence or lentiviruses expressing tdTomato alone as a control. Hippocampal sections from the mice were immunolabeled for HA and stained with DAPI at P35. Low-magnification images (left panels) show the distribution of the HA-tagged nanobody along the CA1 dendritic region. High-magnification 60 \times images of a dendrite in the S. oriens (right panels) show that the HA-tagged Homer1 nanobodies are enriched in dendritic spines labeled with tdTomato. The tdTomato alone condition controls for background HA staining. The Homer1c Nb7 was used in all in vivo experiments since it exhibited the highest degree of overlap with endogenous Homer1c (Dong et al., 2019). (g) Dendritic spine images without 3D reconstructions from Fig. 5 d.

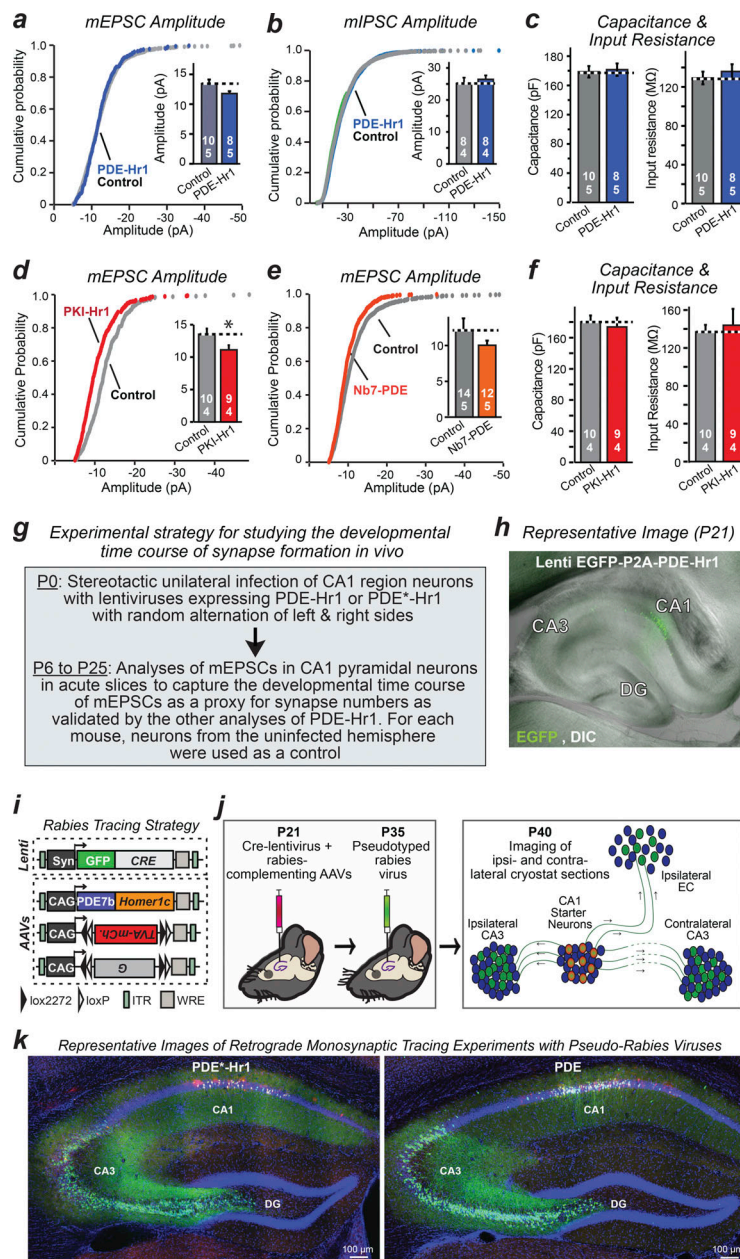


Figure S5. **Additional electrophysiological characterization of the effects of in vivo expression of SynTAMs on the synaptic properties of CA1 pyramidal neurons and further representative images of the hippocampus for rabies virus retrograde tracing experiments.** (a and b) SynTAMs have only a modest effect on mEPSC (a) or mIPSC (b) amplitudes. Measurements are from experiments in Fig. 6, a and b. (c) Capacitance and membrane resistance values for the neurons analyzed in Fig. 6 a. (d) Expression of PKI-Hr1 in CA1 pyramidal neurons modestly decreases mEPSC amplitude. Measurements are from experiments in Fig. 6 c. (e) Same as a and d, except for Nb7-PDE expression experiments. Data are from experiments in Fig. 6 d. (f) Capacitance and membrane resistance measurements of control neurons and neurons expressing the PKI-Homer1 fusion protein in vivo. Data are from experiments in Fig. 6 c. (g) Experimental strategy for monitoring the effect of SynTAMs on the developmental time course of synapse formation in vivo. CA1 neurons of newborn P0 C57BL/6 mice were unilaterally sparsely infected with lentiviruses expressing SynTAMs or controls, and mEPSC recordings were conducted as a proxy for functional synapses at the indicated developmental time points after infection (P6–P25). This approach captured the significant surge of excitatory synapse formation peaking at P10 followed by synapse elimination (Fig. 6, e–i). (h) Representative image of an acute slice of the hippocampus illustrating lentiviral (Lenti) infection. (i and j) Experimental approach used to deconstruct the effect of SynTAMs on synaptic circuit assembly. (i) Diagram of lentiviral and AAV shuttle vectors used for rabies tracing experiments. (j) Overview of experimental manipulations. Neurons of the mouse CA1 region were unilaterally infected at P21 with three viruses (AAVs encoding Cre-inducible mCherry-tagged receptor and packaging proteins for pseudotyped rabies viruses; AAVs encoding Control empty viral particles or PDE-Hr1, PDE*-Hr1, or PDE alone; lentiviruses encoding Cre-recombinase). The same CA1 region was infected subsequently at P35 with pseudotyped rabies viruses encoding EGFP; EGFP-positive cells in the CA1 region, the ipsilateral and contralateral CA3 regions, and the entorhinal cortex were quantified at P40. (k) Representative overviews of hippocampi from retrograde rabies virus–tracing experiments. Starter cells in the CA1 region express both mCherry and EGFP, while presynaptic CA1 and CA3 neurons express only EGFP. Numerical data in a–f are means ± SEM (numbers of cells/experiments). Statistical significance was assessed by two-tailed Student’s t test or two-way ANOVA with post hoc Tukey tests (*, $P < 0.05$). DIC, differential interference contrast; EC, entorhinal cortex; ITR, inverted terminal repeats; Syn, synapsin; TVA-mCh., TVA-mCherry fusion; WRE, woodchuck response element.